Numerical analysis of ellipsometric critical adsorption data

Dan S. P. Smith and Bruce M. Law
Department of Physics, Kansas State University, Manhattan, Kansas 66506-2601

Martin Smock
Fachbereich Physik, Universität Essen, D-45117 Essen, Germany

David P. Landau
Center for Simulation Physics, University of Georgia, Athens, Georgia 30602

(Received 19 August 1996)

A recent study [Dan S. P. Smith and Bruce M. Law, Phys. Rev. E **54**, 2727 (1996)] presented measurements of the ellipsometric coefficient at the Brewster angle $\overline{\rho}$ on the liquid-vapor surface of four different binary liquid mixtures in the vicinity of their liquid-liquid critical point and analyzed the data analytically for large reduced temperatures t. In the current report we analyze this $(\overline{\rho},t)$ data numerically over the entire range of t. Theoretical universal surface scaling functions $P_{\pm}(x)$ from a Monte Carlo (MC) simulation [M. Smock, H. W. Diehl, and D. P. Landau, Ber. Bunsenges. Phys. Chem. **98**, 486 (1994)] and a renormalization-group (RG) calculation [H. W. Diehl and M. Smock, Phys. Rev. B **47**, 5841 (1993); **48**, 6470(E) (1993)] are used in the numerical integration of Maxwell's equations to provide theoretical $(\overline{\rho},t)$ curves that can be compared directly with the experimental data. While both the MC and RG curves are in qualitative agreement with the experimental data, the agreement is generally found to be better for the MC curves. However, systematic discrepancies are found in the quantitative comparison between the MC and experimental $(\overline{\rho},t)$ curves, and it is determined that these discrepancies are too large to be due to experimental error. Finally, it is demonstrated that $\overline{\rho}$ can be rescaled to produce an approximately universal ellipsometric curve as a function of the single variable $\xi_{\pm}/\lambda$, where ξ is the correlation length and λ is the wavelength of light. The position of the maximum of this curve in the one-phase region, $(\xi_{+}/\lambda)_{\mathrm{peak}}$, is approximately a universal number. It is determined that $(\xi_{+}/\lambda)_{\mathrm{peak}}$ is dependent primarily on the ratio $c_{+}/P_{\infty,+}$, where $P_{+}(x)\cong c_{+}x^{-\beta/\nu}$ for $x\ll 1$ and $P_{+}(x)\cong P_{\infty,+}e^{-x}$ for $x\gg 1$. This enables the experimental estimate of $c_{+}/P_{\infty,+}=0.90\pm 0.24$, which is significantly large compared to the MC and RG values of 0.577 and 0.442, respectively. [S1063-651X(97)01001-5]

PACS number(s): 68.10.−m, 64.60.Fr, 05.70.Fh, 82.65.Dp

I. INTRODUCTION

Critical adsorption occurs at the liquid-vapor or liquid-solid surfaces in a critical binary liquid mixture when the bulk critical temperature T_c is approached from the one-phase side, and from the two-phase side provided a wetting layer does not form. For small reduced temperatures $t=|T-T_c|/T_c\ll 1$, the thickness of the adsorption profile is scaled by the diverging bulk correlation length $\xi_{\pm}=\xi_{0\pm}t^{-\nu}$, where the subscript $+$ $(-)$ will be used to indicate one-phase (two-phase) quantities. Let L and H denote the two molecular components of the mixture, where L (H) represents the pure component with the lower (higher) density. The local order parameter is defined on the liquid side of the surface $(z\geqslant 0)$ by

$$m(z,t)=\varphi_L(z,t)-\varphi_L(+\infty,0), \tag{1}$$

where $\varphi_L(z,t)$ is the local volume fraction of the L component expressed as a function of t and z, the depth into the liquid, while $\varphi_L(+\infty,0)$ is the bulk critical volume fraction. For the case in which L is preferentially adsorbed at the liquid-vapor surface (which requires that the surface tension of L is lower than the surface tension of H) the critical adsorption profile scales as [1–5]

$$m_{\pm}(z,t)=M_{-}t^{\beta}P_{\pm}\left(\frac{z+z_e}{\xi_{\pm}}\right). \tag{2}$$

The surface scaling functions $P_{+}(x)$ and $P_{-}(x)$ have different forms, but are both universal. Here β and M_{-} are the usual critical exponent and coefficient of the bulk order parameter in the two-phase region $m_{-}(+\infty,t)=M_{-}t^{\beta}$. The extrapolation length z_e is nonuniversal and independent of z. The surface scaling functions have the limits [3–5]

$$P_{\pm}(x)-P_{\pm}(\infty)\cong P_{\infty,\pm}e^{-x} \tag{3}$$

for $x\gg 1$, with $P_{+}(\infty)=0$ and $P_{-}(\infty)=1$, and

$$P_{\pm}(x)\cong c_{\pm}x^{-\beta/\nu} \tag{4}$$

for $x\ll 1$, where $P_{\infty,\pm}$ and $c_{\pm}$ are universal constants. The values of c_{+} and c_{-} are dependent through the relation [4]

$$\frac{c_{+}}{c_{-}}=\left(\frac{\xi_{0+}}{\xi_{0-}}\right)^{-\beta/\nu}, \tag{5}$$

where the correlation length amplitudes have the universal ratio [6]

$$\xi_{0+}/\xi_{0-}\cong 1.96. \tag{6}$$

TABLE I. Theoretical and experimental values for parameters related to the universal surface scaling functions $P_{\pm}(x)$. The asymptotic power law of Eq. (4) and the exponential decay of Eq. (3) are accurate to within a few percent for $x<x_1$ and $x>x_2$, respectively. The parameters $c_{\pm}$, $P_{\infty,\pm}$, $\int P_{+}$, and $\int P_{-}$ are defined in Eqs. (4), (3), (7a), and (7b), respectively.

		x_1	x_2	c_{+}	c_{-}	$P_{\infty,+}$	$P_{\infty,-}$	$\int P_{+}$	$\int P_{-}$
Theory	RG [a]	0.5	3	0.717	1.113	1.621	$0.208+0.0098x$ [b]	1.91	1.44
	MC [c]	0.2	1	0.866	1.22	1.5	1.0	2.18	1.97
	Interpolation [d]			0.94 ± 0.05	1.24 ± 0.05			2.27 ± 0.33	1.84 ± 0.33
Experiment	Optical [d]			0.955 ± 0.08				2.5 ± 0.5	2.53
	Optical [e]							1.97 ± 0.08	1.65 ± 0.13

[a]Reference [4].
[b]Because the zeroth-order term $P_{\infty,-}=0.208$ is so small, the first-order correction of $0.0098x$ has been included.
[c]Reference [5].
[d]Reference [8].
[e]Reference [24].

Recent theories have provided values for $P_{\infty,\pm}$ and $c_{\pm}$ as well as numerical determinations of $P_{\pm}(x)$ in the crossover region between the limits of large and small x. Diehl and Smock [4] have published a renormalization-group (RG) one-loop calculation for $P_{\pm}(x)$, while Smock, Diehl, and Landau [5] have fitted functions $P_{\pm}(x)$ to the Monte Carlo (MC) data of Landau and Binder [7]. In addition, Flöter and Dietrich [8] have provided universal quantities related to critical adsorption with an interpolation to dimension $d=3$ from exact calculations for $d=2$ and $d=4$. Table I lists the values for $P_{\infty,\pm}$, $c_{\pm}$, and some other relevant parameters from these three theories. The numbers x_1 and x_2 are defined such that the asymptotic forms of $P_{\pm}(x)$ given in Eqs. (3) and (4) hold for $x>x_2$ and $x<x_1$, respectively. The universal critical adsorption integrals $\int P_{\pm}$ are defined by

$$\int P_{+}=\int_0^{\infty} P_{+}(x)dx \tag{7a}$$

and

$$\int P_{-}=\int_0^{\infty}[P_{-}(x)-1]dx. \tag{7b}$$

These integrals are a scaled measure of the total excess adsorption in the one-phase and two-phase regions. Numerical values for the RG and MC surface scaling functions $P_{\pm}(x)$ in the crossover region $x_1<x<x_2$ are provided in Tables II and III. The MC numerical values in Table III were calculated from the Monte Carlo data reported in Refs. [5] and [7] by use of the least-squares B-spline approximation with four knots in order to provide smooth surface scaling functions $P_{\pm}(x)$. The functions $P_{\pm}(x)$ from the RG and MC theories were compared graphically in Ref. [9].

There is a long list of published experimental studies of critical adsorption at the vapor and solid surfaces of liquid mixtures and at the solid surfaces of pure fluids. The experimental probes that have been used include ellipsometry [9–25], optical reflectivity [26,27], evanescent wave fluorescence [28], volumetry [29], gravimetry [30], surface tension measurements [19,31,32], and neutron reflectivity [33]. Every one of these studies observed that the thickness of the adsorption profile increases dramatically as the mixture approaches T_c. Furthermore, many of them provided strong evidence that real systems obey the scaling laws in Eqs. (2)–(4). Postulated adsorption profiles that incorporate these scaling laws have been shown to give reasonable agreement with optical measurements at the vapor and solid surfaces of critical liquid mixtures and polymer solutions [13,14] [15,18,27,34]. The systematic reanalysis of optical data by Liu and Fisher [34] showed that profiles that violate one or more of these scaling laws have a significantly reduced level of agreement with the measurements. The analysis of Liu and Fisher and nearly all of the optical experiments that preceded their work concentrated on the one-phase region, leav-

TABLE II. Numerical values for the surface scaling functions $P_{\pm}(x)$ in the crossover region $x_1\leq x\leq x_2$, obtained from a one-loop renormalization-group calculation [4].

x	$P_{+}(x)$	x	$P_{-}(x)$
0.5	0.93251	0.5	1.62924
0.6	0.82266	0.6	1.50587
0.7	0.73276	0.7	1.41355
0.8	0.65672	0.8	1.34223
0.9	0.59091	0.9	1.28585
1.0	0.53310	1.0	1.24051
1.1	0.48176	1.1	1.20356
1.2	0.43585	1.2	1.17315
1.3	0.39458	1.3	1.14790
1.4	0.35737	1.4	1.12681
1.5	0.32373	1.5	1.10909
1.6	0.29328	1.6	1.09413
1.7	0.26569	1.7	1.08145
1.8	0.24069	1.8	1.07066
1.9	0.21802	1.9	1.06145
2.0	0.19747	2.0	1.05357
2.1	0.17884	2.1	1.04681
2.2	0.16195	2.2	1.04124
2.3	0.14664	2.4	1.03183
2.4	0.13277	2.6	1.02477
2.6	0.10881	2.8	1.01941
2.8	0.08915	3.0	1.01531
3.0	0.07303		

TABLE III. Numerical values for the surface scaling functions $P_{\pm}(x)$ in the crossover region $x_1<x<x_2$, obtained from a Monte Carlo simulation [5]. Typical uncertainties in the values of $P_{\pm}(x)$ are on the order of 10^{-3}.

x	$P_+(x)$	x	$P_-(x)$
0.20531	1.926	0.20390	2.824
0.22170	1.836	0.22475	2.696
0.23809	1.755	0.24559	2.581
0.25448	1.684	0.26643	2.478
0.27087	1.620	0.28728	2.387
0.28726	1.563	0.30812	2.305
0.30365	1.514	0.32896	2.232
0.32004	1.465	0.34981	2.167
0.33643	1.427	0.37065	2.108
0.35282	1.381	0.39149	2.054
0.36921	1.342	0.41234	2.005
0.38560	1.304	0.43318	1.961
0.40199	1.268	0.45402	1.920
0.41838	1.233	0.47487	1.882
0.43477	1.200	0.49571	1.848
0.45116	1.168	0.51655	1.816
0.46755	1.138	0.53740	1.787
0.48394	1.108	0.55824	1.760
0.50033	1.080	0.57908	1.735
0.51672	1.054	0.59993	1.710
0.53311	1.028	0.62077	1.687
0.54950	1.003	0.64161	1.665
0.56589	0.980	0.66246	1.643
0.58228	0.957	0.68330	1.622
0.59867	0.936	0.70414	1.601
0.61506	0.915	0.72499	1.582
0.63145	0.895	0.74583	1.562
0.64784	0.877	0.76667	1.544
0.66423	0.858	0.78752	1.526
0.68062	0.841	0.80836	1.509
0.69701	0.824	0.82920	1.493
0.71340	0.808	0.85005	1.477
0.72979	0.793	0.87089	1.461
0.74618	0.778	0.89173	1.447
0.76257	0.763	0.91257	1.432
0.77896	0.749	0.93342	1.419
0.79535	0.736	0.95426	1.406
0.81174	0.723	0.97510	1.393
0.82813	0.710	0.99595	1.381
0.84452	0.697		
0.86091	0.688		
0.87730	0.673		
0.89369	0.661		
0.91008	0.649		
0.92647	0.637		
0.94286	0.626		
0.95925	0.615		
0.97564	0.604		
0.99203	0.593		

ing the behavior of the critical adsorption profile in the two-phase region relatively untested. Because the RG and MC theoretical functions $P_{\pm}(x)$ were published after these studies, phenomenological functions with multiple adjustable parameters that satisfied the scaling equations (2)–(4) were formulated for the optical dielectric profile $\epsilon(z,t)$. Flöter and Dietrich [8] have extracted surface scaling functions $P_+(x)$ from the ellipsometry critical adsorption experiments of Findenegg and coworkers [14,15] and from the reanalysis of optical data by Liu and Fisher [34]. These experimental $P_+(x)$ functions scatter widely relative to one another and relative to the theoretical functions, particularly in the crossover region $x\sim 1$ between the two asymptotic limits. This could be due to the fact that the profiles were all formulated with multiple adjustable parameters. From these experimental profiles they obtained the estimates $c_+=0.955\pm 0.08$ and $g_+\simeq 0.75\pm 0.15$, where the amplitude relation $\int P_{\pm}=g_{\pm}/(\nu-\beta)$ gives $\int P_+\simeq 2.5\pm 0.5$. The estimates given here represent the mean value obtained from seven different mixtures, and the uncertainty provided for g_+ is one standard deviation. Flöter and Dietrich were also able to extract the two-phase function $P_-(x)$ from the ellipsometric data on the liquid-vapor surface of a critical liquid mixture measured by Hirtz, Lawnik, and Findenegg [14], from which they obtained $g_-\simeq 0.768$, which gives $\int P_-\simeq 2.53$. This value is from one mixture only, which again leaves the two-phase region relatively untested.

The recent neutron reflectivity experiment of Zhao *et al.* [33] on the liquid-vapor surface of a critical binary liquid mixture verified the scaling of Eq. (4) and measured $\beta/\nu=0.55\pm 0.06$, in agreement with the theoretical value of 0.52. This experiment provided a more stringent test of Eq. (4) than is possible with optical experiments because the neutron reflectivity signal is primarily sensitive to the power-law region very near the surface, while optical experiments probe surface structure at greater depths. Dietrich and Schack [35] discussed methods by which the prefactor c_+ appearing in Eq. (4) could be measured in a neutron or x-ray reflectivity experiment, although to our knowledge this has not been accomplished yet.

Other recent experimental studies on critical adsorption include the paper by Desai, Peach, and Franck [38], which reported optical reflectivity measurements of the liquid-glass surface of a critical liquid mixture in the limit where neither component is preferentially attracted to the surface. In the recent paper by Caylor and Law [25] ellipsometry was used to study critical adsorption at the liquid-vapor surface of five critical polymer solutions in the one-phase region. Mukhopadhyay, Senanayake, Caylor, and Law [39] are currently studying critical adsorption in a critical ionic solution.

In a series of papers, Smith and Law [9,21,23,24] reported the ellipsometric measurements at the liquid-vapor surface as a function of the reduced temperature for a number of critical liquid mixtures, with full data sets taken in both the one-phase and two-phase regions. The *best* data from these papers was presented in Ref. [24] for the critical aniline-cyclohexane (AC), isobutyric acid–water (IW), 2,6 lutidine-water (LW), and nitrobenzene-hexane (NH) mixtures. The data analysis used in these papers provided strong confirmation for Eq. (2) in both the one-phase and two-phase regions, and values for the universal integrals $\int P_{\pm}$ were statistically

fitted for each mixture. The experimental values determined for the integrals in Ref. [24] are given in Table I. An important shortcoming of this analysis is that its range of validity is restricted to the ellipsometric data at large reduced temperatures $t \gtrsim 10^{-3}$, while the data are resolved down to $t \sim 10^{-5}$. The purpose of the current paper is to provide a highly sensitive test of the surface scaling functions $P_{\pm}(x)$ derived in the RG theory and the MC simulation with an analysis of the ellipsometric data for the mixtures AC, IW, LW, and NH that is valid over the entire range of reduced temperatures. This is acheived by a graphical comparison of this ellipsometric data with ellipsometric curves calculated numerically [36,37] from the RG and MC surface scaling functions. The fact that these theoretical $P_{\pm}(x)$ functions have zero adjustable parameters allows a much stronger test than was possible in previous papers [13,14,18,34], which were forced to test surface scaling functions with multiple adjustable parameters.

In Sec. II we describe the assumptions used in our calculations of the theoretical ellipsometric curves. The theoretical ellipsometric curves are presented in Sec. III and compared with the experimental data. In Sec. IV it is demonstrated that the ellipsometric curves can be rescaled such that they become approximately universal over a certain range, while an explanation for this universal behavior is provided in the Appendix. Results from Sec. IV are used in Sec. V to make an inference on the true value of the universal ratio $c_+ / P_{\infty,+}$. Finally, a summary is provided in Sec. VI.

II. THEORETICAL $(\overline{\rho},t)$ CURVES

Phase-modulated ellipsometry [40] is a particularly effective method for probing the order-parameter profile. A procedure established by Beaglehole [41] is to moniter the coefficient of ellipticity at the Brewster angle, defined by

$$\overline{\rho} = \mathrm{Im}(r_p / r_s)|_{\theta_B}, \tag{8}$$

where r_p and r_s are the complex reflection coefficients for the two independent polarizations. The coefficient $\overline{\rho}$ has contributions from both the static intrinsic profile expressed in Eqs. (1) and (2) and the thermally generated capillary wave fluctuations [42]. Marvin and Toiga [43] have shown that for light reflecting off a surface for which both the thickness of the static intrinsic profile and the amplitude of capillary wave oscillations are small compared to the wavelength of light ($\lambda = 633$ nm), the contributions to $\overline{\rho}$ from the capillary waves and the intrinsic profile are additive. Thus the ellipsometric measurement on the liquid-vapor surface of a liquid mixture can be written

$$\overline{\rho} = \overline{\rho}_{\mathrm{CW}} + \overline{\rho}_{\mathrm{IP}}, \tag{9}$$

where $\overline{\rho}_{\mathrm{CW}}$ is the capillary wave contribution and $\overline{\rho}_{\mathrm{IP}}$ is the intrinsic profile contribution. For thin surface profiles compared to λ the contribution of the static intrinsic surface profile to the ellipsometric coefficient $\overline{\rho}$ is described by the Drude equation [44]

$$\overline{\rho}_{\mathrm{IP}} = -\frac{\pi}{\lambda} \frac{\sqrt{\epsilon(+\infty,t)+\epsilon(-\infty,t)}}{\epsilon(+\infty,t)-\epsilon(-\infty,t)} \times \int_{-\infty}^{+\infty} \frac{[\epsilon(z,t)-\epsilon(+\infty,t)][\epsilon(z,t)-\epsilon(-\infty,t)]}{\epsilon(z,t)} dz, \tag{10}$$

where $\epsilon(z,t)$ is the optical dielectric profile of the reflecting medium. The Drude equation (10) is valid only for surface profile thicknesses that are thin compared to λ. Since z is scaled by ξ in Eq. (2), this corresponds to $\xi \ll \lambda$, which occurs far from T_c. For thicker profiles (smaller reduced temperatures), Maxwell's equations can be solved numerically [36,37] to derive the $(\overline{\rho}_{\mathrm{IP}},t)$ curve, which would be predicted from a postulated theoretical static intrinsic profile $\epsilon(z,t)$. The capillary wave contribution will be discussed below.

In Ref. [24], $(\overline{\rho},t)$ measurements on the liquid-vapor surface of the critical mixtures AC, IW, LW, and NH were presented. Equation (10) was used to derive the nearly exact result

$$\overline{\rho} = \overline{\rho}_{\mathrm{BG}} - \frac{\pi}{\lambda} f_{\epsilon}(t)(\eta_L - \eta_H) M_- \xi_{0\pm} \left(\int P_{\pm} \right) t^{\beta-\nu}, \tag{11}$$

where η_L and η_H are defined in Eq. (13) below and $f_{\epsilon}(t)$ is the weakly varying function of t defined in Eq. (A4) of Ref. [9]. The background term $\overline{\rho}_{\mathrm{BG}}$ is also nearly independent of t. It contains terms from many different contributions [24] that vary significantly with large changes in temperature, but vary only slightly in the small range of temperatures about T_c studied in our experiment. Equation (11) was used to analyze the data at large reduced temperatures and the experimental values given in Table I for the universal integrals $\int P_{\pm}$ were determined.

In the current manuscript, an algorithm for the numerical integration of Maxwell's equations is employed to derive RG and MC theoretical $(\overline{\rho}_{\mathrm{IP}},t)$ curves, which can be compared directly with the data for the mixtures AC, IW, LW, and NH from Ref. [24] over the entire range of reduced temperatures. The justification for neglecting the capillary wave contribution $\overline{\rho}_{\mathrm{CW}}$ will be provided below. The algorithm of Law and Beaglehole [37], which is a modification of the Born and Wolf algorithm [36], will be used for the numerical integration. All the numerical $\overline{\rho}_{\mathrm{IP}}$ values will be calculated with an accuracy of better than $\pm 5 \times 10^{-6}$ over the entire range of reduced temperatures. As a comparison, our experimental $\overline{\rho}$ values were measured with a typical uncertainty of 2×10^{-5}.

The numerical derivation of a theoretical $(\overline{\rho},t)$ curve requires the development of a theoretical optical dielectric profile $\epsilon(z,t)$. We will use the profile developed in Refs. [9,24], which we now summarize. The static intrinsic profile at the liquid-vapor surface of a liquid mixture consists of both a composition profile and the variation of the total number density of molecules from its effectively zero value in the bulk vapor to the much denser bulk liquid value. The composition profile will be referred to as the critical profile and is confined to the liquid side ($z \geq 0$) of the surface. It is expressed quantitatively in terms of the local order parameter

TABLE IV. Nonuniversal bulk parameters required for the analysis of the four critical liquid mixtures studied in this paper.

Mixture	ϵ_L [a]	ϵ_H [a]	M_-	ξ_{0+} (Å)	$\varphi_L(+\infty,0)$ [b]	T_c (Kelvin) [b]
AC	2.035	2.5163	1.03 ± 0.03 [c]	2.3 ± 0.2 [d]	0.592	303.049 ± 0.003
IW	1.94	1.773	0.783 ± 0.03 [e]	3.63 ± 0.07 [f]	0.405	299.099 ± 0.003
LW	2.217 [g]	1.773	0.931 ± 0.007 [h]	2.5 ± 0.3 [i]	0.3082	306.579 ± 0.004
NH	1.8909	2.4218	0.770 ± 0.006 [j]	3.1 ± 0.4 [k]	0.623	293.107 ± 0.004

[a]Reference [51], except where noted.
[b]Reference [24].
[c]References [52,53].
[d]References [52,54].
[e]Reference [45].
[f]Reference [52].
[g]Reference [55].
[h]Reference [56].
[i]Reference [57].
[j]References [53,58].
[k]Reference [59].

$m(z,t)$ defined in Eq. (1) and obeys the critical scaling of Eq. (2). The total number density profile will be referred to as the noncritical profile. It becomes very thick as it undergoes critical scaling near the *liquid-vapor* critical point, but near the liquid-liquid critical point in our experiment it is only a few molecular layers thick [24,34].

The local order parameter $m(z,t)$ is commonly converted to the optical dielectric profile $\epsilon(z,t)$ by use of the two-component Clausius-Mossotti relation [45]

$$\varphi_L(z,t)\,\eta_L+[1-\varphi_L(z,t)]\,\eta_H\cong\eta(z,t), \tag{12}$$

where volume changes on mixing, which are typically only 1–2 % for most mixtures, have been neglected. In Eq. (12) for $i=L$ and H,

$$\eta_i=\frac{\epsilon_i-1}{\epsilon_i+2}, \tag{13}$$

ϵ_i is the optical dielectric constant of pure liquid i, and

$$\eta(z,t)=\frac{\epsilon(z,t)-1}{\epsilon(z,t)+2}. \tag{14}$$

In Ref. [9] the Clausius-Mossotti relation (12) was used to convert the critical profile expressed in terms of volume fraction in Eqs. (1) and (2) into an optical dielectric profile

$$\epsilon(z,t)=\frac{1+2[\Delta(z,t)+\eta(+\infty,t)]}{1-[\Delta(z,t)+\eta(+\infty,t)]},\quad z\geqslant 0, \tag{15}$$

where

$$\Delta(z,t)=(\eta_L-\eta_H)M_-t^{\beta}\left[P_{\pm}\left(\frac{z+z_e}{\xi_{\pm}}\right)-P_{\pm}(\infty)\right]. \tag{16}$$

Tabled $P_{\pm}(x)$ values from the RG and MC theories in the range $x_1<x<x_2$ are supplied in Tables II and III, respectively. To construct the functions $P_{\pm}(x)$ over the entire range $0\leqslant x<+\infty$, Eqs. (3) and (4) were used for $x>x_2$ and $x<x_1$, respectively, while linear interpolation was used for $x_1\leqslant x\leqslant x_2$. The values for x_1 and x_2 were chosen such that the asymptotic functions of Eqs. (3) and (4) agreed to within a few percent with the numerical values of $P_{\pm}(x)$ at x_2 and x_1, respectively.

In reality the noncritical profile spans both the liquid and vapor sides of the surface, but for the sake of simplicity it will be confined to the vapor side ($z\leqslant 0$). Since the noncritical profile is very thin compared to the critical profile, simplifying a realistic profile in this manner causes a negligible change in the profile's appearance. In Ref. [24] the Fermi interfacial profile expected in mean-field theory [46] was modified to give the optical dielectric profile

$$\epsilon(z,t)=1+\frac{[\epsilon(0,t)-1][1+e^{-z_e/\xi_v}]}{1+e^{-(z+z_e)/\xi_v}},\quad z\leqslant 0, \tag{17}$$

where the vapor correlation length ξ_v scales the noncritical profile thickness.

Equations (15) and (17) describe the model optical dielectric profile that will be used in the numerical integration of Maxwell's equations. These equations contain many nonuniversal parameters that must be specified for each mixture. The values used for ϵ_L, ϵ_H, M_-, ξ_{0+}, and $\varphi_L(+\infty,0)$ are provided in Table IV. We are relying on literature values for all of these parameters except $\varphi_L(+\infty,0)$. The correlation length amplitude in the two-phase region, ξ_{0-}, was determined by using Eq. (6). To determine $\eta(+\infty,t)$ in Eq. (15), Eqs. (12) and (13) were used with $\varphi_L(+\infty,t)=\varphi_L(+\infty,0)$ in the one-phase region and $\varphi_L(+\infty,t)=\varphi_L(+\infty,0)+M_-t^{\beta}$ in the two-phase region. The surface optical dielectric $\epsilon(0,t)$ can be expressed in terms of the surface volume fraction $\varphi_L(0,t)$ using Eqs. (12)–(14). The extrapolation length z_e appearing in both Eqs. (15) and (17) can also be expressed in terms of $\varphi_L(0,t)$ using Eqs. (1) and (2). If $z_e\ll\xi_{\pm}$, the asymptotic power law of Eq. (4) can be used for $P_{\pm}(x)$ to provide the analytic result

$$z_e=\xi_{0\pm}\left(\frac{\varphi_L(0,t)-\varphi_L(+\infty,0)}{M_-c_{\pm}}\right)^{-\nu/\beta}. \tag{18}$$

TABLE V. The second and third columns provide the liquid-vapor surface tensions for pure L and H, where T is the temperature in degrees Celsius. The fourth column states the surface area per molecule of the liquid mixture. These values allow the surface volume fraction $\varphi_L(0,t)$ to be determined for each mixture using Eq. (20).

Mixture	σ_L [a]	σ_H [a]	α [b]
AC	$27.62-0.1188T$	$44.83-0.1085T$	4.50
IW	$26.88-0.0920T$	$75.83-0.1477T$	2.73
LW	$33.91-0.1159T$	$75.83-0.1477T$	1.90
NH	$20.44-0.1022T$	$46.34-0.1157T$	2.50

[a]Reference [60].
[b]Reference [24].

Outside the applicability of this limit, z_e must be determined from $\varphi_L(0,t)$ numerically using linear interpolation on the values of $P_{\pm}(x)$ provided in Tables II and III. This leaves $\varphi_L(0,t)$ and ξ_v as the only two unknown quantities in Eqs. (15) and (17). Two methods of estimating $\varphi_L(0,t)$ will be discussed below and ξ_v will be left as the only adjustable parameter in the calculation of the theoretical $(\overline{\rho},t)$ curves.

In Ref. [9] it was assumed that the surface layer is pure L, $\varphi_L(0,t)=1$. This assumption is plausible because for each mixture we have studied the liquid-vapor surface tension of pure H, σ_H, is considerably larger than the liquid-vapor surface tension of pure L, σ_L. In Ref. [24], $\varphi_L(0,t)$ was estimated using a statistical mechanical theory and surface tension measurements. In the semiempirical theory of Tamura, Kurata, and Odani [47], the liquid-vapor surface tension of the mixture, σ, is related to $\varphi_L(0,t)$ through the relation

$$\sigma^{1/4}=\varphi_L(0,t)\sigma_L^{1/4}+[1-\varphi_L(0,t)]\sigma_H^{1/4}. \tag{19}$$

The surface volume fraction is determined by the bulk volume fraction $\varphi_L(+\infty,t)$ and the surface tension difference $\sigma_H-\sigma_L$,

$$\frac{\varphi_L(0,t)}{1-\varphi_L(0,t)}=\frac{\varphi_L(+\infty,t)}{1-\varphi_L(+\infty,t)}\exp\left[\frac{\alpha(\sigma_H-\sigma_L)}{k_BT}\right]. \tag{20}$$

Here the parameter α is the area per molecule at the liquid-vapor surface of the mixture. In Ref. [24] α was approximated as a constant and was estimated by comparing measurements of σ for the mixtures AC, IW, LW, and NH with Eqs. (19) and (20). In Table V the values of σ_L, σ_H, and α that were used in Ref. [24] are provided for each mixture so that $\varphi_L(0,t)$ can be determined from Eq. (20).

As discussed above, the $t^{\beta-\nu}$ power law for $\overline{\rho}$ in Eq. (11) holds only for large reduced temperatures $t\gtrsim 10^{-3}$. However, one would expect the constant term $\overline{\rho}_{BG}$ in Eq. (11) to remain constant as $t\to 0$. Any contribution to $\overline{\rho}$ that does not vary significantly over the small temperature range included in the interval $10^{-3}<t<10^{-1}$, over which Eq. (11) is valid, will vary even less in the *very* small temperature range of $t<10^{-3}$.

In Ref. [24] it was shown that the contribution of the noncritical profile to $\overline{\rho}$ is contained in the constant term $\overline{\rho}_{BG}$ of Eq. (11). Figure 1(a) shows three numerical $(\overline{\rho},t)$ curves for the mixture IW. All three curves were calculated

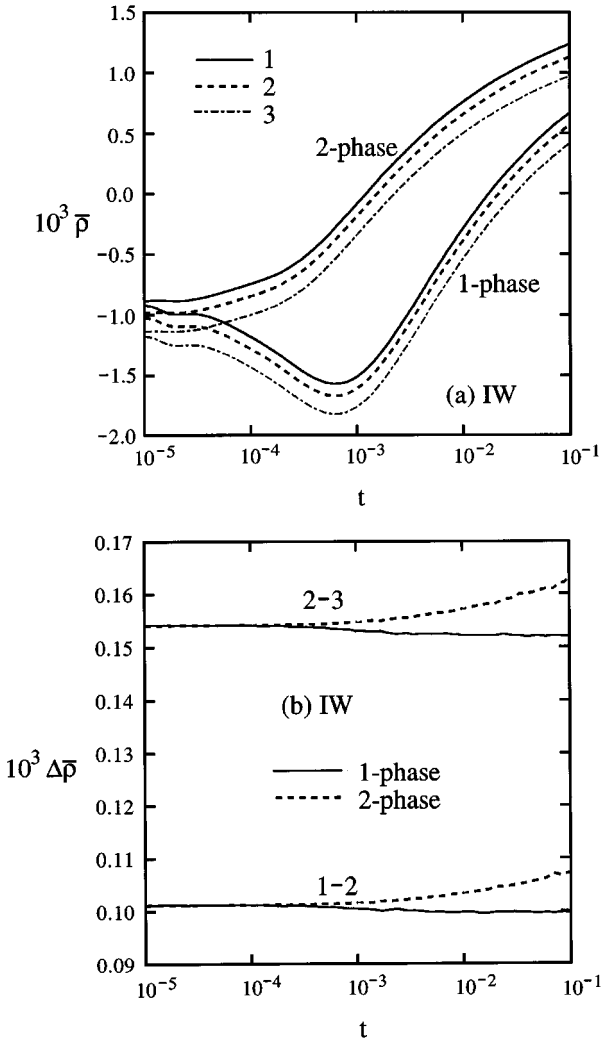

FIG. 1. (a) Semilog plot of three calculations of $\overline{\rho}$, times 1000, as a function of the reduced temperature t in both the one-phase and two-phase regions. The values used for the noncritical correlation length were $\xi_v=3.3$, 3.0, and 2.55 Å for curves 1, 2, and 3, respectively. The MC surface scaling functions $P_{\pm}(x)$ with the condition $\varphi_L(0,t)=1$ and the parameter values for IW in Table IV were used in the calculations. (b) The curves labeled $1-2$ and $2-3$ are the differences in $\overline{\rho}$, $\Delta\overline{\rho}$, between curves 1 and 2 and between curves 2 and 3, respectively, with the one-phase region represented by the solid lines and the two-phase region by the dashed lines.

using the MC $P_{\pm}(x)$ functions and $\varphi_L(0,t)=1$. For the curves labled 1, 2, and 3 the values used for the noncritical correlation length were $\xi_v=3.3$, 3.0, and 2.55 Å, respectively. Figure 1(b) shows the difference $\Delta\overline{\rho}$ between curves 2 and 3 and between curves 1 and 2, labeled $2-3$ and $1-2$, respectively. While $\overline{\rho}$ varies over a range of about 3×10^{-3} for each of the three curves, the difference $\Delta\overline{\rho}$ for any two of the curves only varies by about 10^{-5} over the entire reduced temperature range. This is on the order of the uncertainty in the experimental $\overline{\rho}$ values and is therefore negligible. As expected, this contribution to $\overline{\rho}_{BG}$ remains constant as $t\to 0$. The effect of varying ξ_v is to change the value of $\overline{\rho}_{BG}$ and to raise or lower the $(\overline{\rho},t)$ curve by a constant value without changing its shape. In calculating the theoretical $(\overline{\rho},t)$ curves, ξ_v will be adjusted to give the correct value for

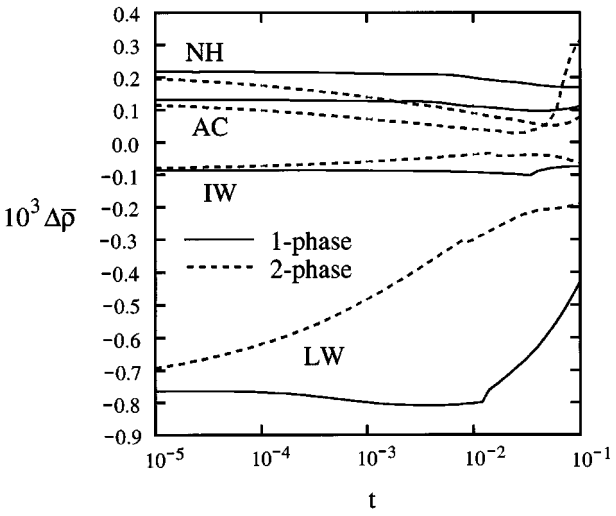

FIG. 2. Semilog plot of the numerically calculated difference $\Delta\overline{\rho}$, times 1000, as a function of the reduced temperature t for the mixtures NH, AC, IW, and LW. The one-phase and two-phase regions are represented by solid and dashed lines, respectively. The difference $\Delta\overline{\rho}$ is $\overline{\rho}$ calculated with $\varphi_L(0,t)=1$ minus $\overline{\rho}$ calculated with $\varphi_L(0,t)$ determined by Eq. (20). In both calculations the MC surface scaling functions $P_{\pm}(x)$ were used along with the parameter values given in Table IV.

$\overline{\rho}_{\rm BG}$, i.e., the value for which the theoretical $(\overline{\rho},t)$ curve is on approximately the same vertical level as the experimental $(\overline{\rho},t)$ curve. The only important comparison we will be able to make between the theoretical and experimental $(\overline{\rho},t)$ curves will be of their shapes, not their vertical levels.

For each of the four mixtures, Fig. 2 shows the difference $\Delta\overline{\rho}$ between a MC theoretical curve calculated with $\varphi_L(0,t)=1$ and a curve calculated with $\varphi_L(0,t)$ determined by Eq. (20). All parameters are otherwise the same for the two curves of each of the four mixtures. In the interval $t<10^{-2}$ all the curves have a variation in $\Delta\overline{\rho}$ on the order of 10^{-4}, except for the two-phase curve of LW, which varies by about 5×10^{-4}. The variation of 10^{-4} is larger than in Fig. 1(b), but is still much too small to affect any of the conclusions drawn below from comparisons between the theoretical and experimental $(\overline{\rho},t)$ curves. With the exception of the two-phase LW curve, switching between the two methods for determining $\varphi_L(0,t)$ has an effect similar to varying the value of ξ_v: it merely changes the value of $\overline{\rho}_{\rm BG}$. As discussed above, the value of $\overline{\rho}_{\rm BG}$ for the theoretical $(\overline{\rho},t)$ curves will be adjusted to give agreement with the experimental data by adjusting the value of ξ_v; this does not affect the important comparison between the *shapes* of the theoretical and experimental curves. All theoretical curves will be calculated with $\varphi_L(0,t)=1$ since Eq. (20) complicates the analysis by introducing the parameters α, σ_L, and σ_H. It should be emphasized, however, that the two-phase LW curve in Fig. 1(b) suggests that under certain circumstances the temperature dependence of $\varphi_L(0,t)$ may have a small but non-negligible influence on the shape of the $(\overline{\rho},t)$ curve.

The previous discussion has neglected the contribution due to capillary wave fluctuations, denoted $\overline{\rho}_{\rm CW}$ in Eq. (9). In Ref. [24] an approximate expression for $\overline{\rho}_{\rm CW}$ was shown to have a variation on the order of 10^{-5} over the range $t\lesssim10^{-2}$. Therefore $\overline{\rho}_{\rm CW}$ is yet another approximately constant contribution to $\overline{\rho}_{\rm BG}$. We will neglect $\overline{\rho}_{\rm CW}$, but its contribution will effectively be included in $\overline{\rho}_{\rm BG}$ by making the appropriate choice for the single adjustable parameter ξ_v.

III. COMPARISON OF EXPERIMENTAL AND THEORETICAL $(\overline{\rho},t)$ CURVES

In Fig. 3 the experimental $(\overline{\rho},t)$ data for the mixtures AC, IW, LW, and NH are compared with the theoretical RG and MC curves generated by the numerical analysis described in Sec. II. The experimental data in the one-phase and two-phase regions are represented by circles and squares, respectively. The MC curves are represented by solid lines, while the RG curves are represented by dashed lines. The parameter values given in Table IV were used in the calculation of the theoretical curves, along with $\varphi_L(0,t)=1$. In Figs. 3(a) and 3(c) the MC curves appear to be discontinuous at T_c. A discontinuity is impossible since both the bulk and the surface phase transitions are continuous. In fact, the one-phase and two-phase region curves were calculated down to $t=10^{-6}$ and it was determined that $\overline{\rho}$ is continuous at T_c.

As discussed in Sec. II, only the comparison between the shapes of the curves is of importance and the comparison between their vertical levels is not meaningful. The values used for the noncritical correlation length were chosen such that the theoretical curves would be on the same vertical level as the experimental curves. The ξ_v values used for AC, IW, LW, and NH, respectively, were 1.7, 3.3, 4.0, and 0.9 Å for the MC curves and 2.5, 2.1, 1.7, and 2.0 Å for the RG curves. As expected, the noncritical profile is found to be only a few molecular layers thick.

The first impression from Fig. 3 is that the experimental, RG, and MC $(\overline{\rho},t)$ curves are in qualitative agreement in all four graphs. The MC theoretical curves are not in perfect agreement with the experimental data, but they compare more favorably than the RG curves do. Some past ellipsometric studies of critical adsorption [14,15,34] have found better agreement of the numerically calculated theoretical curves with the experimental $(\overline{\rho},t)$ data. However, these studies used phenomenological functions for $P_{\pm}(x)$, which had several adjustable parameters, while the MC and RG surface scaling functions have zero adjustable parameters.

Figure 3 provides several comparisons that are more specific than the observation that the MC curves generally fit the experimental data better than the RG curves do. The first such comparison is that for all four mixtures the chosen value of ξ_v simultaneously placed the one-phase and two-phase region MC curves on the same vertical level as their corresponding experimental curves. This simultaneous agreement could not be obtained for the RG curves; different values of ξ_v would be needed to give both the one-phase and two-phase region curves the correct level. It is not clear to us what this infers about the inaccuracy of the RG surface scaling functions.

A second observation is that in all four graphs of Fig. 3 the extremum of $\overline{\rho}$ in the one-phase region occurs at a smaller reduced temperature for the experimental curve than for the RG curve, with the position of the MC curve's peak being in between the two. Much of the discussion in Sec. IV is relevant to this point, while in Sec. V inferences that can

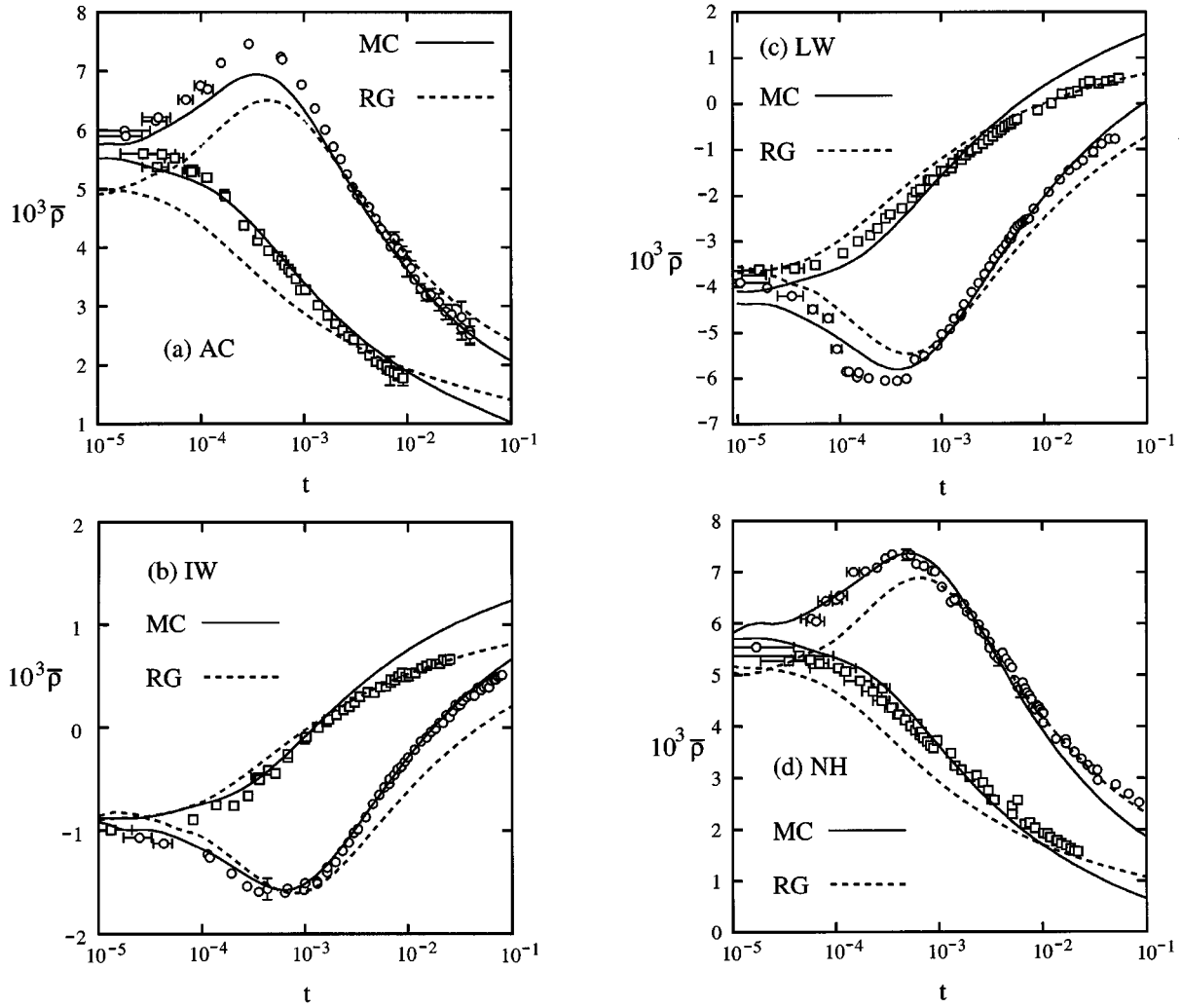

FIG. 3. Semilog plots of $\overline{\rho}$, times 1000, as a function of the reduced temperature t for the critical mixtures (a) AC, (b) IW, (c) LW, and (d) NH. The experimental data are represented by circles in the one-phase region and squares in the two-phase region. Both horizontal and vertical error bars are provided for all data points for which the error bar separation is larger than the width of the circle or square representing it. The numerical calculations of $\overline{\rho}$ using the MC and RG surface scaling functions $P_{\pm}(x)$ are represented by the solid and dashed lines, respectively. The condition $\varphi_L(0,t)=1$ along with the parameter values given in Table IV were used in the calculations.

be drawn from this observation are carefully considered.

The final specific comparison that we will consider is between the slopes of the curves. Equation (11) indicates that for large reduced temperatures the slope of a $\overline{\rho(t)}$ curve is proportional to the universal integrals $\int P_{\pm}$. Closer to T_c this proportionality does not necessarily hold. However, numerical integration of $P_{\pm}(x)$ functions with varying $\int P_{\pm}$ values (see Sec. V) have provided a clear conclusion that holds over the entire range of t: the greater the value of $\int P_+$ or $\int P_-$, the more stretched out the $(\overline{\rho},t)$ curve is in the vertical direction. The values in Table I indicate that the MC $\int P_{\pm}$ values are larger than the RG values. Thus it is not surprising that all the MC curves in Fig. 3 are more stretched out vertically than the RG curves. The experimental values of both $\int P_+$ and $\int P_-$ determined in Ref. [24] and listed in Table I are in between the RG and MC values. Based on this one would expect all the MC (RG) $(\overline{\rho},t)$ curves to be more (less) stretched out vertically than the experimental curves. This trend is followed in Fig. 3, but there are exceptions. The prediction holds for all the RG curves, with the possible exception of the one-phase curve for NH, which is in good agreement with the experimental data for $t>10^{-3}$. Three of the four MC two-phase curves are more stretched out vertically than the experimental curves, with AC being the exception. In the one-phase region the MC curves compare very favorably with the experimental data: the NH curve is too stretched out vertically and the AC curve is under stretched, while the IW and LW curves are in good agreement with their corresponding experimental curves. Thus the conclusions that can be drawn by comparing the slope, or ''vertical stretch,'' of the curves are more or less in line with the conclusions of Ref. [24].

To calculate the theoretical curves graphed in Fig. 3, the parameter values provided in Table IV were used, it was assumed that $\varphi_L(0,t)=1$, and the capillary wave contribution $\overline{\rho}_{\mathrm{CW}}$ was neglected. While the consequences of the latter two approximations were carefully considered in Sec. II, the potential effects of inaccuracies in the measured parameter values in Table IV have not been discussed. The uncertainties in the measured values of T_c are included in the hori-

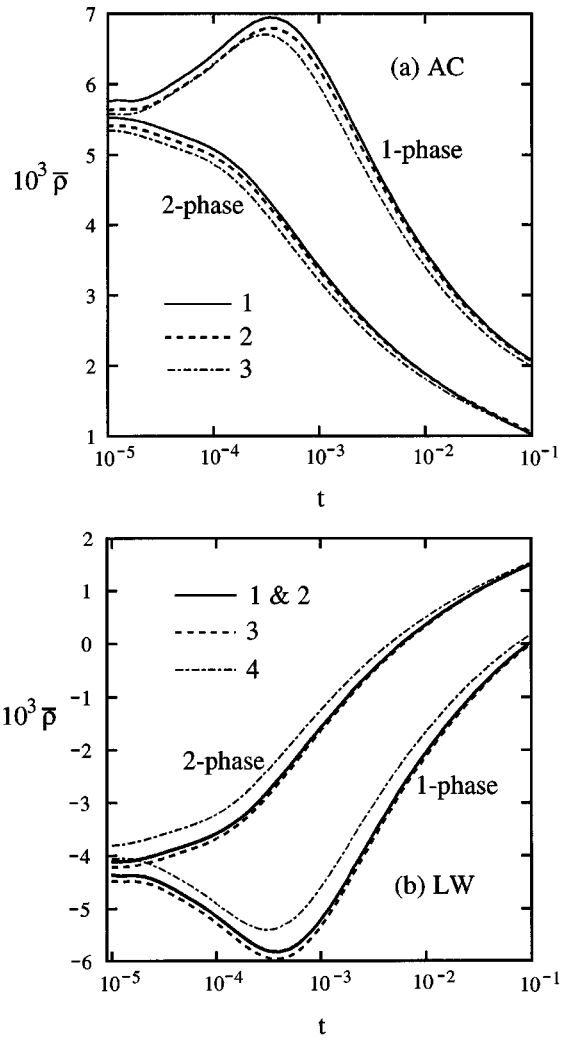

FIG. 4. Semilog plots of $\overline{\rho}$, times 1000, as a function of the reduced temperature t in both the one-phase and two-phase regions. The curves represent numerical calculations of $\overline{\rho}$ using the MC surface scaling functions $P_{\pm}(x)$ and the condition $\varphi_L(0,t)=1$. (a) Curves 1, 2, and 3 were calculated using the parameter values given for the mixture AC in Table IV, with the exceptions of $M_-=1.00$ being used for curve 2 and $\xi_{0+}=2.1$ Å being used for curve 3. (b) Curve 1 was calculated using all the parameter values given for the mixture LW in Table IV. Curve 2, which practically lays on top of curve 1, was calculated using $\varphi_L(\infty,0)=0.3015$. Curves 3 and 4 were calculated using $\epsilon_H=1.766$ and $\xi_{0+}=2.2$ Å, respectively.

zontal error bars of the experimental data points in Fig. 3. To address the uncertainties in the measurements of the other parameters, MC theoretical curves were calculated with the values of ϵ_L, ϵ_H, M_-, ξ_{0+}, and $\varphi_L(+\infty,0)$ increased or decreased relative to the measured values given in Table IV. Figures 4(a) and 4(b) show several of these curves for the mixtures AC and LW. In both figures the curve labeled 1 was calculated without changing any of the values of the parameters in Table IV. Curve 2 in Fig. 4(b), which practically lies on top of curve 1, was calculated for LW with $\varphi_L(+\infty,0)=0.3015$. This is below the measured value by almost eight times the value of its uncertainty given in Table IV, leading us to the conclusion that the measurement of $\varphi_L(+\infty,0)$ was precise enough that its possible inaccuracy is of no concern in the analysis of Fig. 3. Curve 2 of Fig. 4(a) was calculated with the value of M_- decreased to 1.00, which is the minimum of the range of uncertainty for the measured value for AC. The value of t at which the peak of the one-phase curve occurs, t_{peak}, has not changed. However, both the one-phase and the two-phase curves are less stretched out vertically, which is predicted at large reduced temperatures by Eq. (11). Curve 3 of Fig. 4(b) was calculated with $\epsilon_H=1.766$, which is the value of the optical dielectric constant of water at 50 °C, the maximum temperature at which $\overline{\rho}$ was measured for the mixture LW. Again the value of t_{peak} has not changed, but the curve has been stretched out slightly in the vertical direction. A similar result occurs when ϵ_L is varied. Curve 3 of Fig. 4(a) and curve 4 of 4(b) were calculated with the values of ξ_{0+} decreased to 2.1 Å for AC and 2.2 Å for LW, respectively. Equation (5) was used to determine ξ_{0-}, so that the correlation length in the two-phase region has decreased proportionally. Figure 4 shows that ξ_{0+} is the only parameter that changes the value of t_{peak} when its value is varied. For both AC and LW, decreasing the value of ξ_{0+} has decreased the value of t_{peak} and has caused the curves to be less stretched out vertically. The latter effect is predicted at large reduced temperatures by Eq. (11).

Figure 4 leads to the following questions. Could it be that either the RG or MC surface scaling functions are very accurate and the use of incorrect values for the parameters ϵ_L, ϵ_H, M_-, ξ_{0+}, and $\varphi_L(+\infty,0)$ in the calculations of the theoretical (ρ,t) curves are causing a decreased level of agreement with the experimental data in Fig. 3? Is there a set of values for these parameters for each of the four mixtures that would give good agreement between the experimental $(\overline{\rho},t)$ curves and either the RG or MC curves? Would these sets of parameter values be possible, given the actual measured values and their uncertainties?

To answer these questons for the MC one-phase function $P_+(x)$, MC $(\overline{\rho},t)$ curves were calculated with the value of ξ_{0+} being decreased until the value of t_{peak} matched the experimental value. As was pointed out above, this is the only way to change the value of t_{peak}. Next the value of M_- was adjusted until the shape of the MC one-phase curve matched the experimental curve shape. Finally, the value of ξ_v was chosen, which laid the one-phase MC curve on top of the experimental curve. The final MC $(\overline{\rho},t)$ curves are shown along with the experimental curves for each mixture in Figs. 5(a) and 5(b). Excellent agreement between the one-phase curves was achieved for all four mixtures for $t>t_{\text{peak}}$. For AC this agreement continues through T_c and over the entire two-phase curve. For IW the agreement between the two-phase curves is poor for large reduced temperatures, while for LW and NH the agreement ends at t_{peak}. Table VI provides the values of ξ_{0+}, M_-, and ξ_v used in the calculations. The values used for ϵ_L, ϵ_H, and $\varphi_L(+\infty,0)$ were unchanged and are given in Table IV. All four values of ξ_{0+} have decreased relative to the values given in Table IV. With the exception of IW, however, the changes are within the uncertainties of the initial values. The values of M_- have changed by 5.7, 0.4, 7.0, and -11.7 times the values of the uncertainties given in Table IV for the mixtures AC, IW, LW, and NH, respectively. It is highly improbable that three of the four measured values of M_- could be so inaccurate.

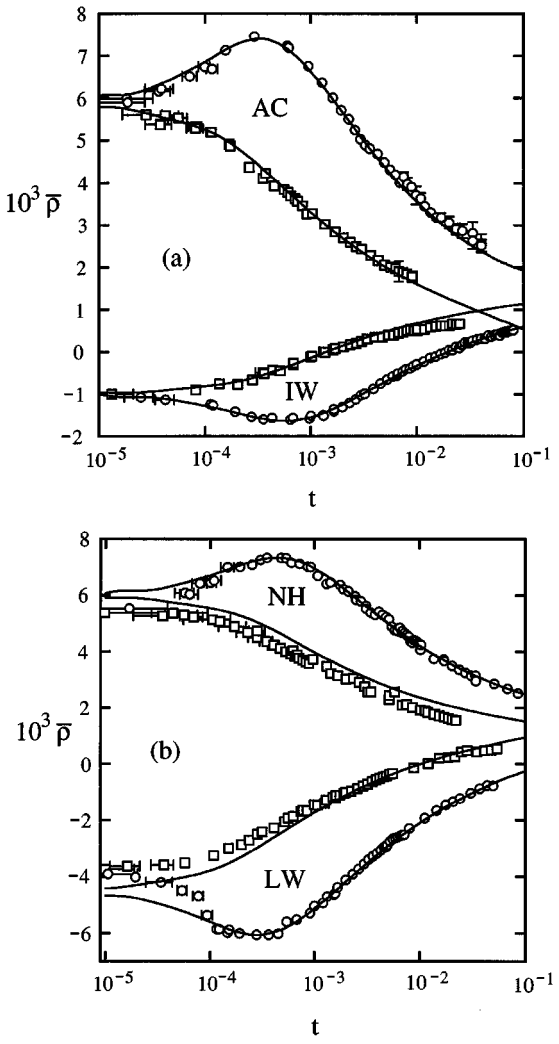

FIG. 5. Semilog plots of $\overline{\rho}$, times 1000, as a function of the reduced temperature t for the critical mixtures (a) AC and IW and (b) LW and NH. The experimental data are represented by circles in the one-phase region and squares in the two-phase region. The solid lines represent $\overline{\rho}$ values that were numerically calculated using the MC surface scaling functions $P_{\pm}(x)$, the condition $\varphi_L(0,t)=1$, and the measured values of ϵ_H, ϵ_L, and $\varphi_L(\infty,0)$ given in Table IV. The values used for ξ_{0+} and M_- were chosen to give the best possible agreement between the one-phase theoretical $(\overline{\rho},t)$ curves and the experimental data.

Instead of varying the values of M_- to reach the correct shapes of the MC curves, the values of ϵ_L or ϵ_H could have been varied. Realistic changes in the values of M_- and ϵ_H produced curve 2 of Fig. 4(a) and curve 3 of Fig. 4(b), respectively. The amount of change that these two cases produced in the shape of the $(\overline{\rho},t)$ curves was about the same. It would be necessary to change the values of ϵ_L or ϵ_H by equally improbable amounts in order to obtain the same level of agreement that is observed in Figs. 5(a) and 5(b). Thus we conclude that the MC function $P_+(x)$ is not in quantitative agreement with our experimental data. We point out once again, however, that Fig. 3 shows qualitative agreement between the behavior of the MC, RG, and experimental $(\overline{\rho},t)$ curves for all four mixtures.

If this method were to be repeated in order to obtain agreement between the one-phase RG $(\overline{\rho},t)$ curves and the experimental data, the changes in the values of M_- and ξ_{0+} would be even more improbable. This is proven by the following argument. Figure 3 shows that the $t_{\rm peak}$ values for the RG curves would have to be decreased even more than was necessary for the MC curves. This would require all four ξ_{0+} values to be decreased by a greater amount than was necessary for the MC curves, thus increasing the unlikelihood. A decrease in the value of ξ_{0+} causes a theoretical curve to become less stretched out vertically. Figure 3 shows that the RG $(\overline{\rho},t)$ curves are initially less stretched out vertically than the MC curves, and the larger decrease in the RG values for ξ_{0+} would increase this disparity. For the MC curves of the mixtures AC, IW, and LW, the M_- values had to be increased in order to stretch the $(\overline{\rho},t)$ curves out vertically to match the shapes of the experimental curves. To achieve this agreement the RG values of M_- would have to be increased by even larger, more improbable amounts for these three mixtures. Thus the RG function $P_+(x)$ is also clearly not in quantitative agreement with our experimental data.

Such clear conclusions cannot be reached for the two-phase theoretical MC and RG functions $P_-(x)$. Without an extremum in the two-phase $(\overline{\rho},t)$ curves, there is nothing analogous to $t_{\rm peak}$, which requires a unique value of ξ_{0-} in order to reach agreement between the theoretical and experimental curves. This agreement could be reached with a range of values of ξ_{0-} and M_-.

TABLE VI. Values used in the numerical calculations of the $(\overline{\rho},t)$ MC theoretical curves graphed in Figs. 5(a) and 5(b). These values were chosen to give the best possible agreement between the one-phase MC curves and the experimental data. See the text for details. The value given in parenthesis after each ξ_{0+} and M_- entry states the difference between the value of this entry and the corresponding measured value given in Table IV, in units of the uncertainty of the measured value.

Mixture	ξ_{0+} (Å)	M_-	ξ_v (Å)
AC	2.2 (−0.5)	1.20 (5.7)	1.3
IW	3.4 (−3.3)	0.795 (0.4)	3.0
LW	2.1 (−1.3)	0.98 (7.0)	2.5
NH	2.8 (−0.75)	0.70 (−11.7)	2.8

IV. UNIVERSAL ELLIPSOMETRIC CURVES

There are many well-known examples [48] in which a universal bulk scaling law is the underlying cause of a universal experimental curve, where measured bulk quantities have been rescaled in order to provide a graph in which different data sets all fall on a single universal curve. However, we are unaware of any examples in the literature in which a universal experimental curve is the result of a surface scaling law such as Eq. (2). Although the scaling in Eq. (2) has a dramatic effect on the behavior of $\overline{\rho}$ for measurements of critical adsorption, rescaling the $(\overline{\rho},t)$ data in order to achieve a universal ellipsometric curve is far from trivial. This is due to the fact that ellipsometry measures a complicated integral of the surface composition profile that cannot be expressed analytically except in certain limits [e.g., Eq. (10)]. In this section we examine a method of rescaling the

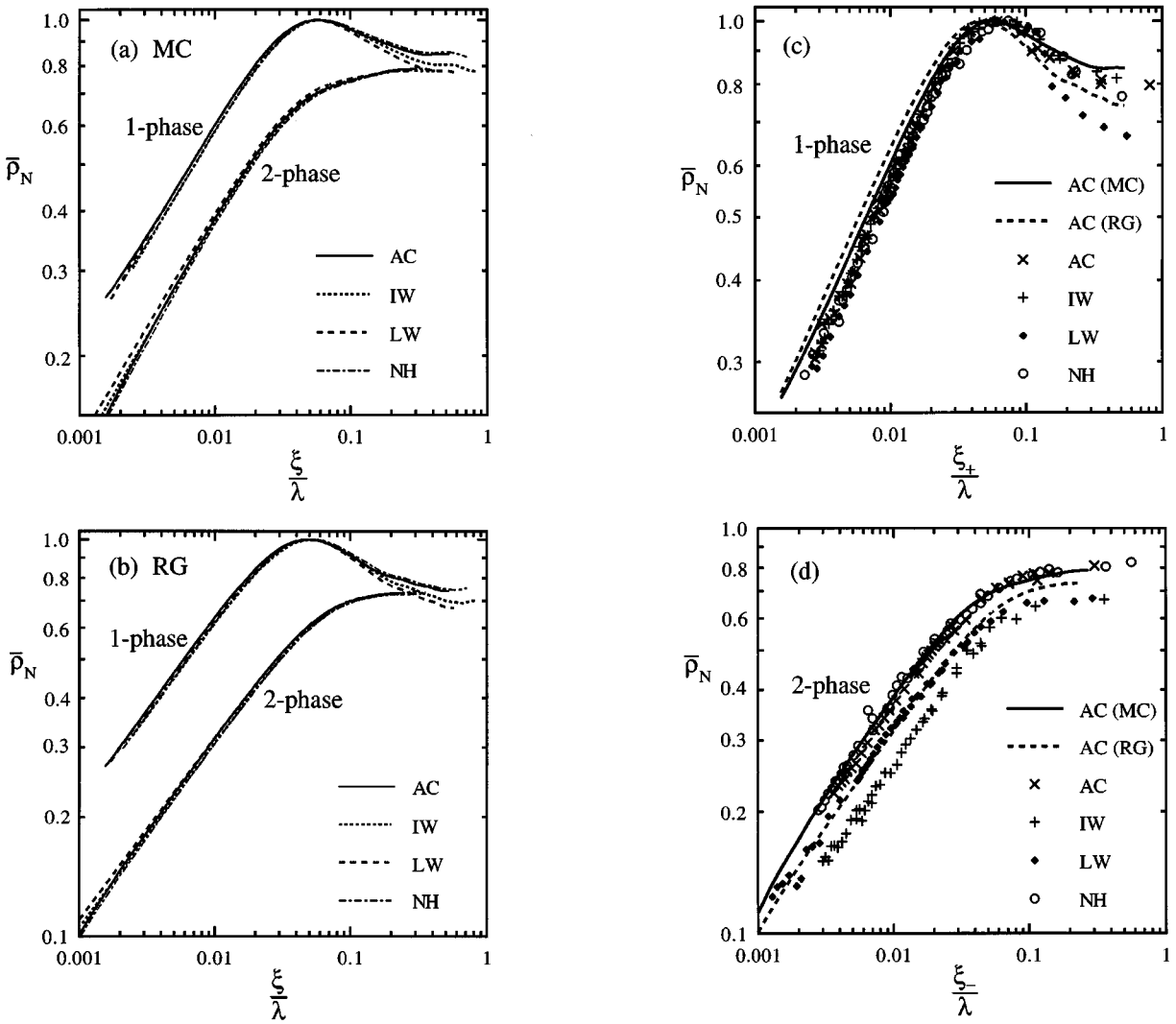

FIG. 6. log-log plots of $\overline{\rho_N}$ [defined in Eq. (21)] as a function of ξ/λ for each of the four mixtures, as labeled on the graphs. (a) MC and (b) RG theoretical curves are shown in both the one-phase and two-phase regions. The experimental curves are shown in the (c) one-phase and (d) two-phase regions, along with the MC and RG curves of the mixture AC for comparison.

$(\overline{\rho},t)$ data in order to produce an experimental curve that is approximately universal. In the Appendix we provide an explanation of how this approximately universal curve is the result of the surface scaling law in Eq. (2).

When $\overline{\rho}-\overline{\rho}_{\mathrm{BG}}$ is plotted as a function of t, the curve in the one-phase region always has an extremum. Since $\overline{\rho}_{\mathrm{BG}}$ is nearly a constant, this fact can be seen in Figs. 3(a)–3(d). The value of $\overline{\rho}-\overline{\rho}_{\mathrm{BG}}$ at the extremum and its position will be denoted $(\overline{\rho}-\overline{\rho}_{\mathrm{BG}})_{\mathrm{peak}}$ and t_{peak}, respectively. There is a large range in the values of both $(\overline{\rho}-\overline{\rho}_{\mathrm{BG}})_{\mathrm{peak}}$ and t_{peak} for the four liquid mixtures, regardless of whether the experimental, MC, or RG curves are being compared. However, if $\overline{\rho}-\overline{\rho}_{\mathrm{BG}}$ is normalized by its extremum value in the one-phase region,

$$\overline{\rho_N}=\frac{\overline{\rho}-\overline{\rho}_{\mathrm{BG}}}{(\overline{\rho}-\overline{\rho}_{\mathrm{BG}})_{\mathrm{peak}}}, \tag{21}$$

and $\overline{\rho_N}$ is plotted as a function of ξ/λ rather than t, the resultant curve is approximately universal in both the one-phase and two-phase regions. This is shown for the MC and RG theoretical curves in Figs. 6(a) and 6(b), respectively. In both figures there is a small (but definitely resolved) spread between the curves of the four mixtures for $\xi_+/\lambda < (\xi_+/\lambda)_{\mathrm{peak}}$, where $(\xi_+/\lambda)_{\mathrm{peak}}$ is the value of ξ_+/λ at the extremum in the one-phase region. This spread becomes larger for $\xi_+/\lambda > (\xi_+/\lambda)_{\mathrm{peak}}$ in the one-phase region. This is also observed for the one-phase experimental data in Fig. 6(c). While the theoretical two-phase $(\overline{\rho_N},\xi_-/\lambda)$ curves in Figs. 6(a) and 6(b) are also approximately universal, Fig. 6(d) shows that the experimental curves are quite spread out in the two-phase region. This large spread is discussed briefly in the Appendix, but its cause is not understood. The MC and RG curves of the mixture AC are also plotted in Figs. 6(c) and 6(d) for comparison.

In the one-phase region both $\overline{\rho_N}$ and the function g_3 discussed in the Appendix are equal to $\overline{\rho}-\overline{\rho}_{\mathrm{BG}}$ divided by a constant. Thus the maxima of $\overline{\rho_N}$ and g_3 occur at the same value of ξ_+/λ, denoted $(\xi_+/\lambda)_{\mathrm{peak}}$. The only clear conclusion that can be reached from the graphical comparisons in Figs. 6(c) and 6(d) is that the values of $(\xi_+/\lambda)_{\mathrm{peak}}$ are largest

TABLE VII. MC, RG, and experimental values of $(\xi_+/\lambda)_{\text{peak}}$ for each mixture. The mean value for the four mixtures is provided in the final row, with an uncertainty of one standard deviation. The uncertainties of the theoretical determinations for each mixture are all approximately 0.0005, while the experimental uncertainties are approximately 0.01.

Mixture	MC	RG	Experiment
AC	0.0564	0.0480	0.060
IW	0.0602	0.0518	0.067
LW	0.0562	0.0492	0.078
NH	0.0607	0.0516	0.075
Mean	0.0584 ± 0.0024	0.0502 ± 0.0019	0.070 ± 0.008

for the experimental curves, smallest for the RG curves, and in between for the MC curves. The MC, RG, and experimental values of $(\xi_+/\lambda)_{\text{peak}}$ are given in Table VII for each mixture. The differences between the MC values of $(\xi_+/\lambda)_{\text{peak}}$ for the different mixtures are definitely real rather than being due to a lack of numerical precision. This is also true for the RG values. Thus $(\xi_+/\lambda)_{\text{peak}}$ is nearly, but not exactly, a universal number.

It was noted in a preliminary report [25] that the $(\overline{\rho_N}, \xi_+/\lambda)$ curves and the value of $(\xi_+/\lambda)_{\text{peak}}$ are approximately universal when applied to a homologous series of critical polymer solutions. In this preliminary report estimates were obtained for the correlation length amplitude (ξ_{0+}) and the polymer index (n) that occur in the expression for the correlation length of a critical polymer solution,

$$\xi = \xi_{0+} N^n t^{-\nu}, \tag{22}$$

where N is the polymer chain length.

The mean values of $(\xi_+/\lambda)_{\text{peak}}$ for the RG and MC theories and for the experimental data are given with errors of one standard deviation in Table VII. These mean values provide a clear contrast between the two theories and the experimental data. This strong contrast is essential to the validity of the conclusions in Sec. V.

V. INFERENCE ON THE VALUE OF THE RATIO $c_+/P_{\infty,+}$

In Sec. IV it was observed that $(\xi_+/\lambda)_{\text{peak}}$ is approximately a universal number, i.e., that its value varies only slightly with changes in the nonuniversal parameters ϵ_L, ϵ_H, $\varphi_L(+\infty,0)$, M_-, and $\xi_{0\pm}$. Furthermore, it was observed that the values of $(\xi_+/\lambda)_{\text{peak}}$ are smaller for the RG curves than the MC curves and are considerably smaller for the MC curves than for the experimental curves. What does this imply about the inaccuracies of the RG and MC surface scaling functions $P_+(x)$? One of the observations in Sec. III provides a hint. It was observed that the values of t_{peak} for the numerically integrated $(\overline{\rho}, t)$ curves change negligibly when M_- is varied without changing the value of ξ_{0+} or the other nonuniversal parameters. From Eq. (2) it can be noted that in the one-phase region varying M_- is equivalent to holding M_- constant while varying the surface scaling function $P_+(x)$ by a multiplicative factor that is independent of x. This implies that if $P_{\infty,+}$ and c_+ appearing in Eqs. (3) and (4) are varied such that the ratio $c_+/P_{\infty,+}$ *remains constant*, the values of t_{peak} and $(\xi_+/\lambda)_{\text{peak}}$ for each mixture change negligibly. In this section we will show that $(\xi_+/\lambda)_{\text{peak}}$ is primarily dependent on the value of $c_+/P_{\infty,+}$ and that this fact can be used to make an inference on the value of $c_+/P_{\infty,+}$.

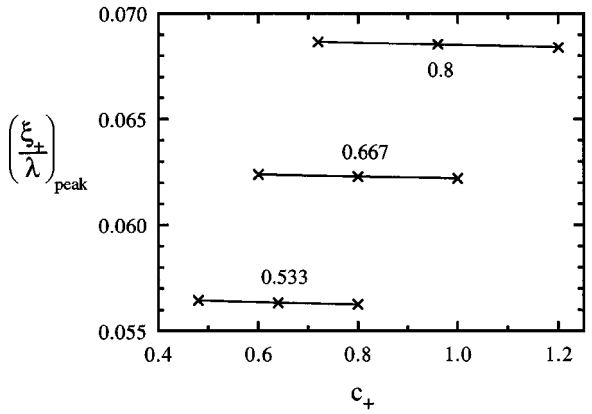

FIG. 7. Position of the maximum in the one-phase region of the universal ellipsometric curve, plotted as a function of c_+. The $(\xi_+/\lambda)_{\text{peak}}$ values were calculated for the mixture IW using the phenomenological surface scaling function given in Eq. (23). The calculated $[c_+, (\xi_+/\lambda)_{\text{peak}}]$ pairs are represented by $\times$'s. The $[c_+, (\xi_+/\lambda)_{\text{peak}}]$ pairs that were calculated with the same value of $c_+/P_{\infty,+}$ are connected by a line and the value of $c_+/P_{\infty,+}$ is given beside the line.

The MC and RG theoretical $P_+(x)$ functions offer only two values for the ratio $c_+/P_{\infty,+}$. To thoroughly test the dependence of $(\xi_+/\lambda)_{\text{peak}}$ on $c_+/P_{\infty,+}$, we will use a phenomenological function $P_+(x)$ that allows c_+ and $P_{\infty,+}$ to be varied arbitrarily. The function we will use for this purpose is Liu and Fisher's ''power law-exponential'' profile [34]

$$P_+(x) = c_+ \left[\frac{1}{x} + \left(\frac{c_+}{P_{\infty,+}} \right)^{-\nu/\beta} \right]^{\beta/\nu} e^{-x}. \tag{23}$$

The notation in Eq. (23) differs somewhat from Liu and Fisher's notation and has been chosen so that Eq. (23) is consistent with Eqs. (3) and (4). This profile may or may not be accurate enough to provide quantitatively correct $(\overline{\rho}, t)$ curves, but we see no reason why it should not provide qualitatively correct conclusions on the dependence of $(\xi_+/\lambda)_{\text{peak}}$ on the ratio $c_+/P_{\infty,+}$. Figure 7 shows a plot of the peak position $(\xi_+/\lambda)_{\text{peak}}$ versus c_+ for nine different $(\overline{\rho}, t)$ curves calculated using the nonuniversal parameter values given in Table IV for the mixture IW and Liu and Fisher's surface scaling function in Eq. (23). The nine data points in Fig. 7 are grouped into three sets of three, with each set having a different $c_+/P_{\infty,+}$ value. The three data points in each set are joined by a line and are labeled by their value of $c_+/P_{\infty,+}$. The graph shows that $(\xi_+/\lambda)_{\text{peak}}$ is nearly independent of c_+ as long as $c_+/P_{\infty,+}$ is held constant, but changing the value of $c_+/P_{\infty,+}$ changes the value of $(\xi_+/\lambda)_{\text{peak}}$ significantly. More specifically, $(\xi_+/\lambda)_{\text{peak}}$ increases when $c_+/P_{\infty,+}$ is increased.

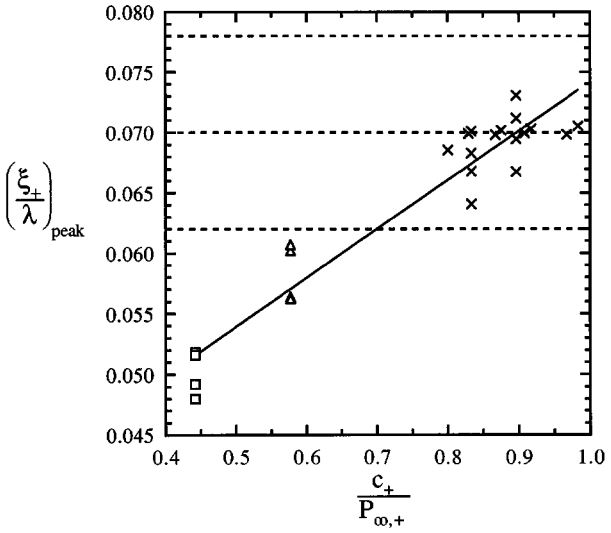

FIG. 8. Calculated peak position of the one-phase ellipsometric curve $(\xi_+/\lambda)_{peak}$ as a function of the ratio $c_+/P_{\infty,+}$. The four squares and four triangles represent calculations for each of the four mixtures using the RG and MC scaling functions $P_+(x)$, respectively. The 16 $\times$'s represent four calculations for each of the four mixtures using the phenomenological profile in Eq. (23). The middle dashed line represents the experimental value of $(\xi_+/\lambda)_{peak}=0.070$, while the outer two dashed lines represent its range of uncertainty 0.070 ± 0.008. The solid line represents a linear regression fit to all 24 of the calculated data points in the graph.

In Fig. 8 the peak position $(\xi_+/\lambda)_{peak}$ is plotted as a function of $c_+/P_{\infty,+}$ for a large number of numerically integrated $(\overline{\rho},t)$ curves. The four squares and four triangles represent calculations for each of the four mixtures using the RG and MC scaling function $P_+(x)$, respectively. The middle and outer dashed lines represent the experimental value of $(\xi_+/\lambda)_{peak}=0.070$ and its range of uncertainty of 0.070 ± 0.008. The 16 crosses, clustered around the experimental value of $(\xi_+/\lambda)_{peak}=0.070$, represent four calculations for each of the four mixtures using the phenomenological scaling function in Eq. (23). The 4 crosses for each mixture form a diagonal line that is approximately parallel to the solid line in the graph. There is a significant variation in the value of $(\xi_+/\lambda)_{peak}$ when the same value of $c_+/P_{\infty,+}$ is used for the four mixtures. As discussed in Sec. IV, $(\xi_+/\lambda)_{peak}$ is approximately, but not exactly, a universal number. Despite this fact, the general trend is clear in Fig. 8: $(\xi_+/\lambda)_{peak}$ increases as $c_+/P_{\infty,+}$ increases, regardless of whether the RG, MC, or phenomenological profile is used in the calculation. The graph suggests that the RG and MC values for $c_+/P_{\infty,+}$ are both too low. In order to quantify this, linear regression was used to fit all 24 data points in Fig. 8 (including the points calculated using the RG, MC, and phenomenological profiles) to the relationship

$$\left(\frac{\xi_+}{\lambda}\right)_{peak}=a+b\left(\frac{c_+}{P_{\infty,+}}\right). \tag{24}$$

This linear relationship is suggested by Fig. 8, where a line is formed by the four points calculated for each mixture using the phenomenological profile. Because we have no knowledge of the actual relationship between $(\xi_+/\lambda)_{peak}$ and $c_+/P_{\infty,+}$, we have no justification for considering a mathematical model that is more complicated. The parameter values obtained from the fit to the data points shown in Fig. 8 are $a=0.034\pm0.002$ and $b=0.040\pm0.003$ and Eq. (24) is represented by the solid line in the figure. Equation (24) can be inverted to provide the relationship

$$\left(\frac{c_+}{P_{\infty,+}}\right)=A+B\left(\frac{\xi_+}{\lambda}\right)_{peak}, \tag{25}$$

where $A=-0.83\pm0.07$ and $B=25\pm2$. If the experimental value of $(\xi_+/\lambda)_{peak}=0.070\pm0.008$ is used in Eq. (25), one obtains

$$\left(\frac{c_+}{P_{\infty,+}}\right)=0.90\pm0.24. \tag{26}$$

The uncertainty in this determination contains contributions from both the uncertainty of the experimental value of $(\xi_+/\lambda)_{peak}$ and the uncertainties of A and B. The latter two uncertainties are a result of the calculated points in Fig. 8 being spread out around the solid line, which, in turn, is due to the small dependence of $(\xi_+/\lambda)_{peak}$ on the nonuniversal mixture parameters.

Our experimental estimate in Eq. (26) is surprisingly large in comparison to the MC and RG values of $c_+/P_{\infty,+}=0.577$ and 0.442, respectively. We add the caution that the determined value in Eq. (26) could be different if an alternative phenomenological profile were to be used in place of Eq. (23). This has not been checked because the procedure for determining $c_+/P_{\infty,+}$ from a phenomenological profile outlined above requires considerable computational effort. It is interesting to note that in their analysis of the data from three optical experiments, Liu and Fisher [34] estimated an even larger value of $c_+/P_{\infty,+}\simeq1.18$. We are unaware of any other existing theoretical or experimental determinations of this ratio in the literature.

VI. SUMMARY

We have analyzed the ellipsometric data presented in Ref. [24], which was measured on the liquid-vapor surface of four different binary liquid mixtures in the vicinity of their liquid-liquid critical point. Various theoretical universal surface scaling functions $P_\pm(x)$ were used in the numerical integration of Maxwell's equations to provide theoretical $(\overline{\rho},t)$ curves that could be compared directly with the experimental data in both the one-phase and two-phase regions and over the entire range of reduced temperatures. Both the MC surface scaling functions of Smock, Diehl, and Landau [5] and the RG functions of Diehl and Smock [4] provided $(\overline{\rho},t)$ curves that were in qualitative agreement with the experimental data. The MC curves were generally found to be in better quantitative agreement with the data than the RG curves. However, systematic discrepancies were found in the quantitative comparison between the MC and experimental $(\overline{\rho},t)$ curves, and it was determined that these discrepancies are too large to be due to experimental error.

It was demonstrated that $\overline{\rho}$ could be rescaled to provide the quantities $\overline{\rho_N}$ and g_3, defined in Eqs. (21) and (A4), respectively, which are universal (or approximately univer-

sal) functions of the single variable $\xi_\pm/\lambda$ for $\xi_\pm/\lambda \ll 1$. Both $\overline{\rho_N}$ and g_3 possess a maximum in the one-phase region and their maxima have the common position $(\xi_+/\lambda)_{\text{peak}}$. The values of $(\xi_+/\lambda)_{\text{peak}}$ are given for the MC and RG theories and for the experimental data in Table VII, where it can be noted that $(\xi_+/\lambda)_{\text{peak}}$ is approximately, but not exactly, a universal number. The value of $(\xi_+/\lambda)_{\text{peak}}$ provides a strong contrast between the RG, MC, and experimental ellipsometric curves. Finally, it was determined that $(\xi_+/\lambda)_{\text{peak}}$ is primarily dependent on the ratio $c_+/P_{\infty,+}$, where the functional relationship is depicted in Fig. 8. This enabled us to obtain the experimental estimate of $c_+/P_{\infty,+}=0.90\pm0.24$. This can be compared with Liu and Fisher's [34] experimental estimate of 1.18 and with the determinations of 0.577 and 0.442 from the MC and RG theoretical studies, respectively.

In closing we note that it would be worthwhile to repeat this ellipsometric study while varying the wavelength of light, especially at longer wavelengths where the critical scattering from the bulk would be less. This would provide an alternative route to testing the universality of the $\overline{\rho_N}$ curves, which are predicted to scale as ξ/λ. It would also assist us in deducing a more accurate experimental determination of the ratio $c_+/P_{\infty,+}$.

ACKNOWLEDGMENTS

We wish to thank Professor H. W. Diehl for his guidance. This work was supported by the National Science Foundation through Grants No. DMR-9208123 and No. DMR-9500827.

APPENDIX: EXAMINATION OF THE CAUSE OF THE UNIVERSAL ELLIPSOMETRIC CURVES

In Sec. IV it was demonstrated that when $\overline{\rho_N}$, defined in Eq. (21), is plotted as a function of ξ/λ, the resultant curve is approximately universal in both the one-phase and two-phase regions. In Figs. 6(a)–6(d), graphs of $(\overline{\rho_N},\xi/\lambda)$ are presented. In this appendix we outline an explanation for why these curves are approximately universal.

In theory, the coefficient of ellipticity $\overline{\rho}$ can be determined from the optical dielectric profile of the surface being studied $\epsilon(z,t)$ by solving Maxwell's equations. This solution of $\overline{\rho}$ would, in general, be a function of integrals of functions of $\epsilon(z,t)$, with the variable of integration being z/λ. Equation (10) and the more specific Eq. (11), which hold only when $\xi \ll \lambda$, provide examples of such a solution. It can be noted from Eqs. (12)–(16) that $\epsilon(z,t)$ for $z>0$ is a universal function of the variables $(\eta_L-\eta_H)M_-t^\beta$, $\epsilon(+\infty,t)$, and $(z+z_e)/\xi_\pm$ for the critical liquid mixtures we are studying. As discussed in Sec. II, $\overline{\rho}-\overline{\rho}_{\text{BG}}$ is not expected to have a dependence on the parameter z_e nor on the noncritical profile [$\epsilon(z,t)$ for $z<0$]. Thus we expect $\overline{\rho}-\overline{\rho}_{\text{BG}}$ to be a universal function of the variables $(\eta_L-\eta_H)M_-t^\beta$, $X_2=\epsilon(+\infty,t)$, and $X_3=\xi_\pm/\lambda$. The variable X_3 is a result of the integration of functions of $\epsilon(z,t)$ with respect to z/λ and the dependence of $\epsilon(z,t)$ on $z/\xi_\pm$. By noting that $(\eta_L-\eta_H)M_-t^\beta=(X_1X_3^{-\beta/\nu})/c_\pm$, where $X_1=c_\pm(\eta_L-\eta_H)M_-(\xi_{0\pm}/\lambda)^{\beta/\nu}$, it can be seen that $\overline{\rho}-\overline{\rho}_{\text{BG}}$ is a universal function of X_1, X_2, and X_3 [49]. Equation (11) becomes a more transparant example of this if it is rewritten as

$$\overline{\rho}-\overline{\rho}_{\text{BG}}=-\pi\left(\frac{\int P_\pm}{c_\pm}\right)X_1 g_2(X_2)X_3^{1-\beta/\nu}, \quad X_3\ll 1, \tag{A1}$$

where $g_2(X_2)=f_\epsilon(t)$ is a universal function of $X_2=\epsilon(+\infty,t)$.

The parameters η_L and η_H, defined in Eq. (13), are functions of only ϵ_L and ϵ_H, respectively. We have neglected the small temperature dependence of ϵ_L and ϵ_H, so that X_1 is independent of t for the theoretical calculations. Equations (12)–(14) indicate that the bulk liquid optical dielectric constant $\epsilon(+\infty,t)$ is a function of ϵ_L, ϵ_H, and $\varphi_L(+\infty,t)$ only. In the one-phase region, $\varphi_L(+\infty,t)=\varphi_L(+\infty,0)$, so that X_2 is also independent of t. The values of X_1 and X_2 are different for each mixture, but in the one-phase region the $(\overline{\rho}-\overline{\rho}_{\text{BG}},t)$ curve for a given mixture can alternatively be expressed as a $(\overline{\rho}-\overline{\rho}_{\text{BG}},X_3)$ curve, with X_1 and X_2 being constant. In the two-phase region, X_2 varies weakly as a function of t.

In Eq. (A1), $\overline{\rho}-\overline{\rho}_{\text{BG}}$ is separable,

$$\overline{\rho}-\overline{\rho}_{\text{BG}}=g_1(X_1)g_2(X_2)g_3(X_3), \tag{A2}$$

where g_1, g_2, and g_3 are universal functions. Equation (A1) holds only in the limit $X_3\ll 1$, but imposes no restrictions on the values of X_1 and X_2. If one postulates that $\overline{\rho}-\overline{\rho}_{\text{BG}}$ is separable as in Eq. (A2) for the entire range of X_1, X_2 and X_3 values, then the functions $g_1(X_1)=-X_1$ and $g_2(X_2)=f_\epsilon(t)$, which can be identified in Eq. (A1), must hold for all values of X_1, X_2, and X_3. Furthermore, the postulate implies that $\overline{\rho}$ can be rescaled to give $g_3(X_3)=(\overline{\rho}-\overline{\rho}_{\text{BG}})/g_1(X_1)g_2(X_2)$, which is a universal function of the single variable $X_3=\xi_\pm/\lambda$. Equation (A1) implies that

$$g_3(\xi_\pm/\lambda)=\pi\left(\frac{\int P_\pm}{c_\pm}\right)(\xi_\pm/\lambda)^{1-\beta/\nu}, \quad \frac{\xi_\pm}{\lambda}\ll 1. \tag{A3}$$

Expressing the above definition of g_3 in terms of the physical quantities provides the result

$$g_3(\xi_\pm/\lambda)=\frac{\overline{\rho}-\overline{\rho}_{\text{BG}}}{c_\pm f_\epsilon(t)(\eta_L-\eta_H)M_-(\xi_{0\pm}/\lambda)^{\beta/\nu}}, \tag{A4}$$

which we use to calculate g_3 for each mixture. In the one-phase region, where $\epsilon(+\infty,t)$ and thus $f_\epsilon(t)$ are independent of t, g_3 is merely $\overline{\rho}-\overline{\rho}_{\text{BG}}$ divided by a nonuniversal constant. In the two-phase region, however, $f_\epsilon(t)$ varies weakly with t. In Figs. 9(a) and 9(b), g_3 is plotted as a function of $\xi_\pm/\lambda$ for the MC and RG calculations in the one-phase and two-phase regions. Since the graphs are log-log plots, the curves follow a straight line with a slope of $1-\beta/\nu$ in the range of ξ/λ over which Eq. (A3) is valid. In this range the calculated $g_3(\xi/\lambda)$ functions are universal, i.e., the curves for each of the four mixtures fall on top of each other in both the one-phase and two-phase regions. For larger values of $\xi_\pm/\lambda$, the g_3 curves begin to deviate from a straight line and the curves of the four mixtures simultaneously begin to separate. This nonuniversality of $g_3(X_3)$ proves that $\overline{\rho}-\overline{\rho}_{\text{BG}}$ is *not* separable as in Eq. (A2), except over the range of applicability of Eq. (A1).

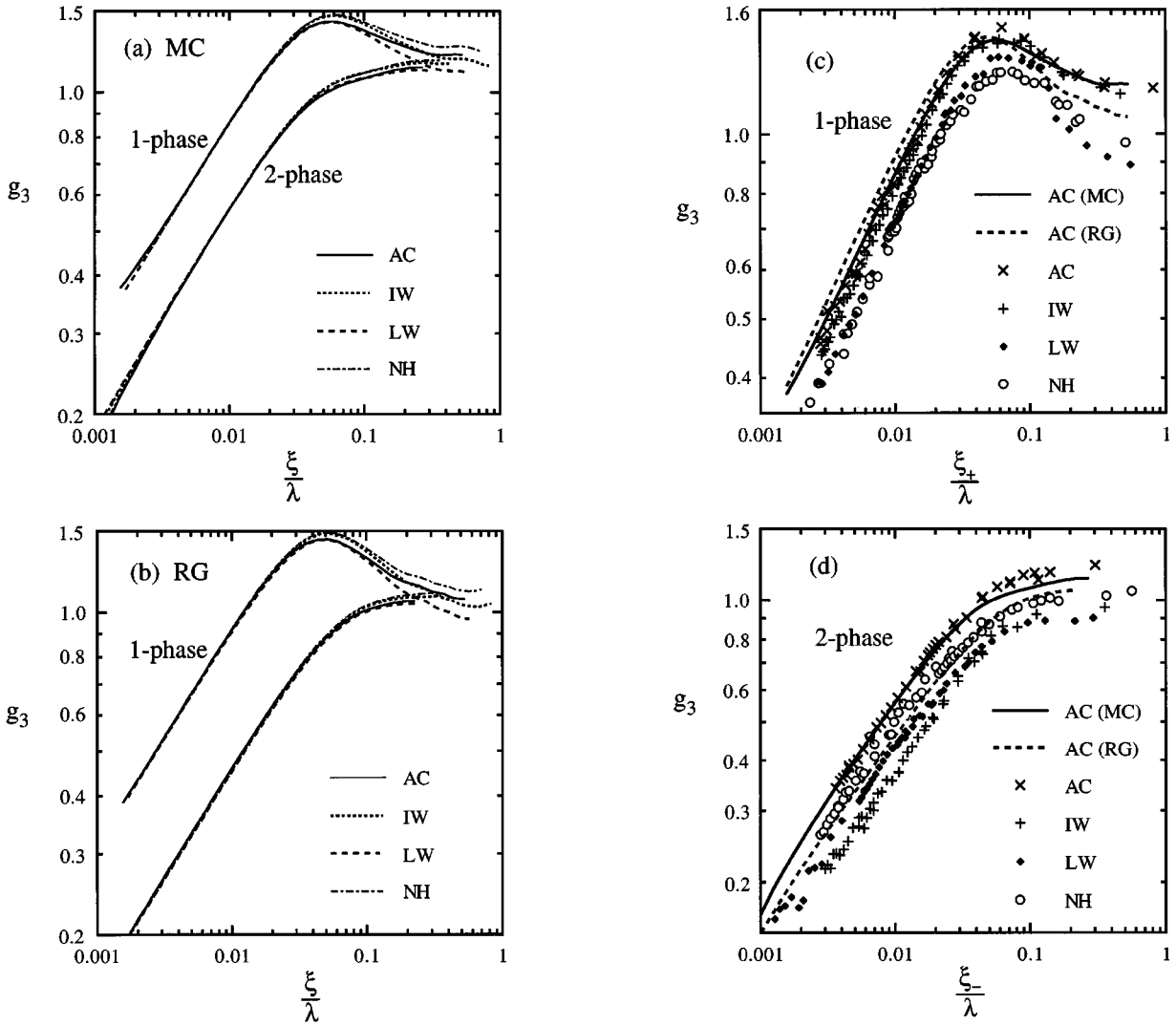

FIG. 9. log-log plots of g_3 [defined in Eq. (A4)] as a function of ξ/λ for each of the four mixtures, as labeled on the graphs. (a) MC and (b) RG theoretical curves are shown in both the one-phase and two-phase regions. The experimental curves are shown in the (c) one-phase and (d) two-phase regions, along with the MC and RG curves of the mixture AC for comparison.

Figures 9(c) and 9(d) show log-log plots of g_3 versus $\xi_\pm/\lambda$ for the experimental data in the one-phase and two-phase regions, respectively. The AC curves from the two theories are also shown for comparison. Unlike the theoretical curves, the experimental curves do not fall on top of each other for $\xi_\pm/\lambda \ll 1$. However, just like the theoretical curves, the experimental curves are linear with the expected slope of $1-\beta/\nu$ for small values of ξ/λ. This indicates that the experimental data are obeying the functional form of Eq. (A3), except that there is a range of values for the prefactors $\pi(\int P_+/c_+)$ and $\pi(\int P_-/c_-)$ for the four different mixtures. The factor of $c_\pm$ in the denominator [49] is present only because the experimental data were divided by it when g_3 was calculated using Eq. (A4). Since the MC values for $c_\pm$ were used in this division for all four mixtures, the apparent spread in the values for $\pi(\int P_\pm/c_\pm)$ in Figs. 9(c) and 9(d) actually indicates a spread in the $\int P_\pm$ values. Equivalent conclusions were reached in Ref. [24], where Eq. (11), which is equivalent to Eq. (A3), was shown to provide a good fit to the experimental data with the expected value of $\beta-\nu$ for $\xi_\pm/\lambda \ll 1$. However, there was a large spread in the fitted values for both $\int P_+$ and $\int P_-$. In both Ref. [24] and Figs. 9(c) and 9(d), the apparent spread in the $\int P_\pm$ values could have been caused by inaccuracies in the measured values of ϵ_L, ϵ_H, $\varphi_L(+\infty,0)$, M_-, and $\xi_{0\pm}$. Of these parameters, the $\xi_{0\pm}$ values are measured with the least precision. This issue is unresolved.

In the one-phase region, both g_3 and $\overline{\rho_N}$ are obtained by dividing $\overline{\rho}-\overline{\rho}_{\rm BG}$ by a nonuniversal constant. For g_3 this constant is a known function of ϵ_L, ϵ_H, $\varphi_L(+\infty,0)$, M_-, $\xi_{0\pm}$, and λ. For $\overline{\rho_N}$, however, $(\overline{\rho}-\overline{\rho}_{\rm BG})_{\rm peak}$ is determined graphically and its dependence on the nonuniversal parameters is unknown. In the two-phase region $\overline{\rho_N}$ is still obtained by dividing $\overline{\rho}-\overline{\rho}_{\rm BG}$ by a constant, while g_3 is obtained by dividing $\overline{\rho}-\overline{\rho}_{\rm BG}$ by a weakly t-dependent quantity.

Figures 6(a) and 6(b) provide log-log graphs of $\overline{\rho_N}$ as a function of ξ/λ for the MC and RG calculations in both the one-phase and two-phase regions. These curves are similar to the curves of g_3 in Figs. 9(a) and 9(b) in that they are universal and follow a straight line for $\xi/\lambda \ll 1$, with the curves

of the four mixtures separating for larger values of ξ/λ. They are dissimilar in that the curves of g_3 for the four mixtures in Figs. 9(a) and 9(b) lay precisely on top of each other over a range of small ξ/λ values, while the $\overline{\rho_N}$ curves for the four mixtures in Figs. 6(a) and 6(b) have a small spread in this range. Also Figs. 9(a) and 9(b) show that the peak value of g_3 in the one-phase region varies slightly from mixture to mixture, while the peak value of $\overline{\rho_N}$ is one for all of the mixtures by definition. These differences eliminate the possibility that $(\overline{\rho}-\overline{\rho_{\rm BG}})_{\rm peak}$ is exactly proportional to the one-phase value of $c_+ f_\epsilon(t)(\eta_L-\eta_H)M_-(\xi_{0+}/\lambda)^{\beta/\nu}$ appearing in Eq. (A4), with the proportionality constant being universal. It is apparent, however, that the proportionality constant between $(\overline{\rho}-\overline{\rho_{\rm BG}})_{\rm peak}$ and $c_+ f_\epsilon(t)(\eta_L-\eta_H)M_-(\xi_{0+}/\lambda)^{\beta/\nu}$ is *approximately* universal. In Fig. 9(a), for example, the maxima of IW and NH in the one-phase region are slightly greater than the maxima of AC and LW. If all four of these curves were divided by their respective maximum value, the curves would be shifted down without changing shape such that the new values for all four maxima would be one. Since the IW and NH curves would be shifted down slightly more than the other two, their curves in the linear $(\xi/\lambda \ll 1)$ region would end up slightly below the AC and LW curves. This is exactly the situation in Fig. 6(a). Thus we conclude that $\overline{\rho_N}$ is approximately universal for $\xi/\lambda \ll 1$ in the one-phase region for two reasons: first, because g_3 is exactly universal in this range and, second, because the maximum value of g_3 in the one-phase region is approximately universal. In addition, $\overline{\rho_N}$ is approximately universal in the two-phase region for the above reasons and because $f_\epsilon(t)$ varies only weakly with t. We have noted that $(\overline{\rho}-\overline{\rho_{\rm BG}})_{\rm peak}$ is approximately proportional to $c_+ f_\epsilon(t)(\eta_L-\eta_H)M_-(\xi_{0+}/\lambda)^{\beta/\nu}$, but can a more accurate relationship between $(\overline{\rho}-\overline{\rho_{\rm BG}})_{\rm peak}$ and the nonuniversal parameters be derived? Our attempts have failed.

A major advantage of $\overline{\rho_N}$ over g_3 can be seen in Fig. 6(c), which provides a log-log plot of the experimental $(\overline{\rho_N},\xi_+/\lambda)$ curves in the one-phase region, along with the MC and RG curves of the mixture AC for comparison. Here, finally, is a universal experimental ellipsometric curve, with the data for the four mixtures lying on top of each other for $\xi/\lambda \ll 1$ [50]. Perhaps the inaccuracies in the values of $c_+ f_\epsilon(t)(\eta_L-\eta_H)M_-(\xi_{0+}/\lambda)^{\beta/\nu}$ that were used are separating the curves in Figs. 9(c) and 9(d), while $(\overline{\rho}-\overline{\rho_{\rm BG}})_{\rm peak}$ is known more accurately because it was determined from the ellipsometric data rather than the measured values of ϵ_L, ϵ_H, $\varphi_L(+\infty,0)$, M_-, and $\xi_{0\pm}$. This does not explain Fig. 6(d), however, which shows that the experimental $(\overline{\rho_N},\xi_-/\lambda)$ curves are quite spread out in the two-phase region. We do not yet understand the cause of the large spread in the experimental curves in Fig. 6(d).

[1] Equation (2) is applicable to the liquid–hard-wall surface and is commonly accepted as being applicable to the liquid-vapor surface. However, it is not rigorously known to hold for the latter case, where capillary waves are present. See, for example, M. E. Fisher and P. J. Upton, Phys. Rev. Lett. **65**, 2402 (1990). Although the capillary wave fluctuations have a small amplitude at the liquid-vapor surface, they are correlated over large distances across the interface. Thus a significant perturbation to Eq. (2) due to coupling between the surface fluctuations and the order parameter fluctuations is possible.

[2] P. Kumar, Phys. Rev. B **10**, 2928 (1974); T. C. Lubensky and M. H. Ruben, *ibid.* **12**, 3885 (1975); K. Binder, in *Phase Transition and Critical Phenomena*, edited by C. Domb and J. L. Lebowitz (Academic, London, 1983), Vol. VIII, p. 1; H. W. Diehl, in *Phase Transitions and Critical Phenomena*, edited by C. Domb and J. L. Lebowitz (Academic, London, 1986), Vol. X, p. 75; K. Ohno and Y. Okabe, Phys. Rev. B **39**, 9764 (1989).

[3] M. E. Fisher and P.-G. de Gennes, C. R. Acad. Sci. Paris B **287**, 207 (1978).

[4] H. W. Diehl and M. Smock, Phys. Rev. B **47**, 5841 (1993); **48**, 6470(E) (1993). The RG values that we are using for c_+, c_-, and $P_{\infty,+}$ were obtained from Diehl and Smock via private correspondence and differ somewhat from the values given in this reference.

[5] M. Smock, H. W. Diehl, and D. P. Landau, Ber. Bunsenges. Phys. Chem. **98**, 486 (1994).

[6] E. Brezin, J. C. Le Guillou, and J. Zinn-Justin, Phys. Lett. **47A**, 285 (1974); H. B. Tarko and M. E. Fisher, Phys. Rev. Lett. **31**, 926 (1973); A. J. Liu and M. E. Fisher, Physica A (Amsterdam) **156**, 35 (1989).

[7] D. P. Landau and K. Binder, Phys. Rev. B **41**, 4786 (1990).

[8] G. Flöter and S. Dietrich, Z. Phys. B **97**, 213 (1995).

[9] D. S. P. Smith and B. M. Law, Phys. Rev. E **52**, 580 (1995). The value of 0.502 given for $\varphi_L(+\infty,0)$ for IW in Table II of this paper was incorrect. The actual value was 0.392.

[10] A. I. Rusanov *Progress in Surface and Membrane Science* (Academic, New York, 1971), Vol. 4, p. 57.

[11] D. Beaglehole, J. Chem. Phys. **73**, 3366 (1980); **75**, 1544 (1981); Phys. Lett. **91A**, 237 (1982); J. Phys. Chem. **87**, 4749 (1983).

[12] B. Heidel and G. H. Findenegg, J. Phys. Chem. **88**, 6575 (1984); J. Chem. Phys. **87**, 706 (1987).

[13] R. Süssmann and G. H. Findenegg, Physica A (Amsterdam) **156**, 114 (1989).

[14] A. Hirtz, W. Lawnik, and G. H. Findenegg, Colloids Surf. **51**, 405 (1990).

[15] A. Hirtz, K. Bonkhoff, and G. H. Findenegg, Adv. Colloid Interface Sci. **44**, 241 (1993).

[16] J. W. Schmidt and M. R. Moldover, J. Chem. Phys. **83**, 1829 (1985).

[17] J. W. Schmidt, J. Chem Phys. **85**, 3631 (1986).

[18] J. W. Schmidt, Phys. Rev. A **41**, 885 (1990).

[19] M. Privat, L. Tenebre, R. Bennes, E. Tronel-Peyroz, J. M. Douillard, and L. Ghaicha, Langmuir **4**, 1151 (1988).

[20] D. Bonn, H. Kellay, and G. H. Wegdam, J. Chem. Phys. **99**, 7115 (1993).

[21] B. M. Law, Phys. Rev. Lett. **67**, 1555 (1991).

[22] B. M. Law, C. M. Sorensen, and F. Zhou, Fluid Phase Equilibria **75**, 225 (1992).

[23] D. S. P. Smith and B. M. Law, J. Chem. Phys. **99**, 9836 (1993).

[24] D. S. P. Smith and B. M. Law, Phys. Rev. E **54**, 2727 (1996).
[25] C. L. Caylor and B. M. Law, J. Chem. Phys. **104**, 2070 (1996). In our preliminary analysis for the present manuscript, $\overline{\rho_N}$ was plotted as a function of $n_B\xi/\lambda$, rather than ξ/λ, where n_B is the bulk index of refraction of the liquid mixture. Our reasoning for this was that λ/n_B is approximately the wavelength of light in the liquid near the surface, so that it would be the appropriate quantity to scale the correlation length. However, the discussion in the Appendix of the current manuscript indicates that ξ/λ is actually the correct parameter to use. In fact, the appearance of the graphs of $\overline{\rho_N}$ versus $n_B\xi/\lambda$ for the mixtures AC, IW, LW, and NH is qualitatively identical to the $\overline{\rho_N}$ versus ξ/λ graphs in Figs. 6(c) and 6(d). Furthermore, the percentage spread in the values of $(n_B\xi/\lambda)_{\rm peak}$ is nearly the same as it is for the $(\xi_+/\lambda)_{\rm peak}$ values. Caylor and Law applied our preliminary results in the analysis of their ellipsometric study of critical adsorption in dilute polymer solutions. Had they used ξ/λ in their analysis, rather than $n_B\xi/\lambda$, their conclusions would not have changed significantly.
[26] C. Franck and S. E. Schnatterly, Phys. Rev. Lett. **48**, 763 (1982); J. A. Dixon, M. Schlossman, X.-L. Wu, and C. Franck, Phys. Rev. B **31**, 1509 (1985); C. Franck, J. Chem. Phys. **82**, 5633 (1985).
[27] M. Schlossman, X.-L. Wu, and C. Franck, Phys. Rev. B **31**, 1478 (1985).
[28] D. Beysens and S. Leibler, J. Phys. (Paris) Lett. **43**, L133 (1982).
[29] S. Blümel and G. H. Findenegg, Phys. Rev. Lett. **54**, 447 (1985).
[30] G. H. Findenegg and R. Löring, J. Chem. Phys. **81**, 3270 (1984).
[31] M. P. Khosla and B. Widom, J. Colloid Interface Sci. **76**, 375 (1980); N. Nagarajan, W. W. Webb, and B. Widom, J. Chem. Phys. **77**, 5771 (1982).
[32] L. Ghaicha, M. Privat, L. Tenebre, R. Bennes, E. Tronel-Peyroz, and J. M. Douillard, Langmuir **4**, 1326 (1988); R. Bennes, M. Privat, E. Tronel-Peyroz, and M. Amara, *ibid.* **7**, 1088 (1991); M. Amara, M. Privat, R. Bennes, and E. Tronel-Peyroz, Europhys. Lett. **16**, 153 (1991); J. Chem. Phys. **98**, 5028 (1993); S. Karad, M. Amara, A. Laouenan, E. Tronel-Peyroz, R. Bennes, and M. Privat, *ibid.* **100**, 1498 (1994).
[33] H. Zhao, A. Penninckx-Sans, L.-T. Lee, D. Beysens, and G. Jannink, Phys. Rev. Lett. **75**, 1977 (1995).
[34] A. J. Liu and M. E. Fisher, Phys. Rev. A **40**, 7202 (1989).
[35] S. Dietrich and R. Schack, Phys. Rev. Lett. **58**, 140 (1987).
[36] M. Born and E. Wolf, *Principles of Optics* (Pergamon, Oxford, 1980), Sec. 1.6.
[37] B. M. Law and D. Beaglehole, J. Phys. D **14**, 115 (1981); B. M. Law, Ph.D. thesis, Victoria University of Wellington, New Zealand, 1985 (unpublished).
[38] N. S. Desai, S. Peach, and C. Franck, Phys. Rev. E **52**, 4129 (1995).
[39] A. Mukhopadhyay, P. Senanayake, C. L. Caylor, and B. M. Law (unpublished).
[40] D. Beaglehole, in *Fluid Interfacial Phenomena*, edited by C. A. Croxton (Wiley, New York, 1986).
[41] D. Beaglehole, Physica B (Amsterdam) **100**, 163 (1980).
[42] F. P. Buff, R. A. Lovett, and F. H. Stillinger, Jr., Phys. Rev. Lett. **15**, 621 (1965).
[43] A. M. Marvin and F. Toigo, Phys. Rev. A **26**, 2927 (1982).
[44] P. K. L. Drude, *The Theory of Optics* (Dover, New York, 1959), p. 292.
[45] W. V. Andrew, T. B. K. Khoo, and D. T. Jacobs, J. Chem. Phys. **85**, 3985 (1986).
[46] J. S. Rowlinson and B. Widom, *Molecular Theory of Capillarity* (Clarendon, Oxford, 1982).
[47] M. Tamura, M. Kurata, and H. Odani, Bull. Chem. Soc. Jpn. **28**, 83 (1955).
[48] H. E. Stanley, *Introduction to Phase Transitions and Critical Phenomena* (Clarendon, Oxford, 1971). For examples of universal experimental curves see p. 10, Fig. 1.8; p. 73, Fig. 5.3; p. 188, Fig. 11.4; and p. 189, Fig. 11.5.
[49] The factor of $c_\pm$ is included in the definition of X_1 so that it will have the same value in the one-phase and two-phase regions according to Eq. (5). To calculate g_3 for the experimental data from the definition in Eq. (A4), the MC values for $c_\pm$ were used. If the true values of $c_\pm$ could be used to determine the experimental g_3 values, the experimental curves in Figs. 9(c) and 9(d) would all be equally shifted up or down without changing shape and the spread in these curves and the values of $(\xi_+/\lambda)_{\rm peak}$ would remain unchanged.
[50] The fact that the four experimental curves in Fig. 6(c) nearly lie on top of each other infers that either all four of the ξ_{0+} values that have been used are accurate, or all four values differ from the true values by a common factor. The second possibility seems unlikely, although it should be emphasized that measured values of ξ_{0+} have been used for AC and IW, but the values used for LW [57] and NH [59] are means of measured values. Assuming that the four ξ_{0+} values that we have used are accurate, Fig. 6(c) suggests a different method for measuring ξ_{0+}: measure $\overline{\rho_N}$ and plot it as a function of $\xi_{0+}t^{-\nu}/\lambda$, with ξ_{0+} being varied until this curve lies on top of the experimental curves in Fig. 6(c).
[51] *CRC Handbook of Chemistry and Physics*, 63rd ed., edited by Robert C. Weast (Chemical Rubber Company, Boca Raton, FL, 1982).
[52] D. Beysens, A. Bourgou, and P. Calmettes, Phys. Rev. A **26**, 3589 (1982).
[53] D. Atack and O. K. Rice, Discuss. Faraday Soc. **15**, 210 (1953).
[54] P. Calmettes, I. Lagues, and C. Laj, Phys. Rev. Lett. **28**, 478 (1972).
[55] D. Beysens and D. Esteve, Phys. Rev. Lett. **54**, 2124 (1985).
[56] M. A. Handschy, R. C. Mockler, and W. J. O'Sullivan, Chem. Phys. Lett. **76**, 172 (1980). The first 15 data points were refitted with $\beta=0.325$ to give $\Delta n=0.288t^{\beta}$.
[57] E. Gulari, A. F. Collings, R. L. Schmidt, and C. J. Pings, J. Chem. Phys. **56**, 6169 (1972). Gulari *et al.* measured 2.0 ± 0.2 and 2.92 ± 0.19 Å for the correlation length amplitude in the one-phase region. We are using the mean $\xi_{0+}=2.5$ Å. There is a related comment in Ref. [50].
[58] G. Zalczer, A. Bourgou, and D. Beysens, Phys. Rev. A **28**, 440 (1983).
[59] J. Rouch, P. Tartaglia, and S. H. Chen, Phys. Rev. A **37**, 3046 (1988). In this reference, $\xi_{0+}=3.54$ Å was measured for NH. In Ref. [58] $\xi_{0+}=2.65$ Å was measured. We are using the mean $\xi_{0+}=3.1$ Å. There is a related comment in Ref. [50].
[60] J. J. Jasper, J. Phys. Chem. Ref. Data **1**, 841 (1972).